Dynamics, wakes, and regime transitions of a fixed angular particle in an unbounded inertial flow. I. Regular tetrahedron angular position

Guodong Gai
Department of Mathematics, University of British Columbia, Vancouver, BC, Canada

Anthony Wachs*
Department of Mathematics, University of British Columbia, Vancouver, BC, Canada and Department of Chemical & Biological Engineering, University of British Columbia, Vancouver, BC, Canada

(Received 27 January 2023; accepted 24 May 2023; published 27 June 2023)

We investigate the unbounded inertial flow of a Newtonian fluid past a fixed regular tetrahedron, the Platonic polyhedron with the lowest sphericity, in the range of Reynolds number $100 \leqslant \mathrm{Re} \leqslant 500$. Three angular positions of the tetrahedron are considered: a face facing the flow (TF), an edge facing the flow (TE), and a vertex facing the flow (TV). We analyze and determine the two well-known regime transitions: loss of symmetry of the wake structures and loss of stationarity of the flow as a function of the Reynolds number Re. In the steady regime, we show that the symmetry of the wake structure is closely related to the number of edges on the particle front surface. For the unsteady flows, we find a new symmetric double-hairpin vortex shedding regime in the edge facing the flow (TE) cases due to its unique angular position. The dominant frequency of this double-hairpin vortex shedding is twice that of the single-hairpin vortex shedding in the flow past a sphere, a cube, or a tetrahedron at other angular positions. Furthermore, we present a force analysis attempting to explain the wake transitions in connection to the drag and lift force evolution. Eventually, we provide the critical Reynolds numbers for the regime transitions from steady to unsteady flows, which are highly dependent on the angular position of the tetrahedron.

DOI: 10.1103/PhysRevFluids.8.064304

I. INTRODUCTION

Multiphase flow is ubiquitous in environmental, biological, and other industrial applications in which rigid particles, droplets, or bubbles of various shapes are carried in a fluid [1–3]. Over the past decades, there have been sustained research activities on the flow interaction with a three-dimensional bluff body due to its importance in, e.g., particulate air pollution [4], river sedimentation [5], ocean dynamics [6], liquid fuel in engines [7], and fire-mitigation spray systems [8]. The interactions between the dispersed and the carrier phase lead to rich and complex flow dynamics.

Numerous studies investigated the basic configuration of a fixed sphere in a unidirectional flow, revealing the intricacy of regime transitions and vortex structures in the particle wake region [9–12]. Due to its omnidirectional symmetry, the sphere has been chosen as an ideal dispersed particle. In 1961, Magarvey *et al.* used dye visualization experiments to investigate the regime transition phenomena of a flow past a sphere [13]. In 1999, a symmetry-breaking process was proposed and explained in the systematic analysis of Johnson *et al.* [14]. They showed good agreements between the experimental results and the numerical results from steady to unsteady flows. Afterward, the instability of the flow in the sphere wake region has been extensively investigated both numerically

*wachs@math.ubc.ca

and experimentally [15,16]. A more complete wake regime transition mechanism was proposed by Jenny *et al.* [17]. The sphere wake flow becomes separated at Re $\approx$ 24, and then an axisymmetric toroidal vortex region appears [9]. This vortex region keeps expanding with increasing Reynolds number until Re $\approx$ 212, where the wake structure undergoes the first regular bifurcation to a planar symmetric state, characterized by a pair of counter-rotating vortex filaments extending downstream of the sphere [17]. Small-amplitude oscillations without vortex shedding were observed experimentally in the wake region at Reynolds number slightly less than Re = 270 [18]. Then, through a secondary Hopf bifurcation [14,19,20], the periodic hairpin vortex shedding turns up, along with the planar symmetric wake structures. Experimental flow visualization shows that the hairpin vortices are always on the same side [21]. However, high-fidelity numerical simulations reveal the two-sided vortex shedding originating from different sources. One side results from the shedding of the vortex ring attached to the rear of sphere [20], and the opposite side is due to the interaction of the near-wake region with the outer flow [14].

It was estimated that at least 70% of the raw material particles used in industries are nonspherical, among which many have angular edges [22]. Flow interaction with a particle of complex geometry such as a cylinder [23,24], an ellipsoid [25,26], or a cube [27,28], has been receiving more and more attention over the past 20 years. For example, the dynamics of the flow past a cube at low and intermediate Reynolds numbers has been the subject of several works [29–32]. Raul *et al.* [33] performed numerical simulations of the flow past a fixed cube in the range of $100 \leqslant \mathrm{Re}_{\mathrm{edge}} \leqslant 400$, where $\mathrm{Re}_{\mathrm{edge}}$ denotes the Reynolds number using the cube edge as the length scale. As the first systematic research, the sequence of regime transitions of a steady laminar flow past a fixed cube was carefully investigated by Saha *et al.* [29,34]. It was reported that the wake conserves symmetry about two orthogonal planes at Reynolds number up to $\mathrm{Re}_{\mathrm{edge}} = 216 \sim 218$. Similar to the flow past a fixed sphere, four pairs of opposite-signed vortices were noticed in the wake region of the cube. Then, two leglike counterrotating vortex threads identified using Q criterion were observed after the first regular bifurcation [29]. The drag coefficient C_d decreases with Re for the investigated flow regimes, and one component of the lift coefficient increases once the symmetry of the wake structure breaks down. Subsequently, Klotz *et al.* [20] studied experimentally the wake transitions behind a cube with a face facing the flow at moderate Reynolds numbers $100 \leqslant \mathrm{Re}_{\mathrm{edge}} \leqslant 400$. Two flow bifurcation mechanisms were confirmed, and the vortices in the wake region were observed to originate from the four rear corners of the cube for the flow regimes studied. Landau's instability model was applied to determine the onset of the two bifurcations based on highly sensitive experimental visualization data. Recently, Meng *et al.* [35] performed highly resolved body-fitting direct numerical simulations for the flow past a fixed isolated cube at small and moderate Reynolds numbers $1 \leqslant \mathrm{Re} \leqslant 400$ to elucidate the physical characteristics of the flow, especially in the particle wake region. Four regimes, including the orthogonal steady-symmetry (OSS), the planar steady-symmetry (PSS), the hairpin-vortex shedding (HS), and the chaotic vortex shedding (CS) regimes were observed and thoroughly discussed. The critical Reynolds numbers of regime transitions were reported to be $\mathrm{Re}_{\mathrm{cr}}^{\mathrm{RT}} = 207$ for the first regular bifurcation and $\mathrm{Re}_{\mathrm{cr}}^{\mathrm{HT}} = 252$ for the Hopf bifurcation.

Unlike the sphere, angular particles will experience forces due to their angularity and angular position in the flow [36]. The effects of the particle shape on drag, lift, and torque coefficients for different nonspherical particles are usually characterized by empirical correlations obtained from experimental or high-fidelity numerical simulation results. Based on experimental data, Haider and Levenspiel [37] established a widely used correlation of the drag coefficient $\overline{C_d}$ for nonspherical particles as a function of the Reynolds number Re and the particle sphericity ϕ, i.e., the ratio between the surface area of the volume equivalent sphere and the surface area of the nonspherical particle. In this correlation, the drag coefficient data of the free-settling tetrahedron are extracted from the experimental measurements of Pettyjohn *et al.* [38]. Regardless of having a good agreement with experimental results, this correlation using only sphericity as an input parameter fails to account for the particle angular position, which has a significant impact on wake flow dynamics [39,40]. Drag coefficients were found to be significantly affected by the orientation of nonspherical particles such as ellipsoids and cubes [26]. Ganser *et al.* [41] extended the work of Ref. [39] and established

an empirical correlation for the drag coefficient $\overline{C_d}$ of isometric particles considering the crosswise sphericity, which is defined as the ratio between the streamwise cross-sectional area of the volume equivalent sphere and that of the nonspherical particle. Based on a similar idea, Hölzer *et al.* [42,43] proposed another correlation for the drag coefficient $\overline{C_d}$ of the nonspherical particles using both crosswise and lengthwise sphericity to consider the particle orientation [38,44]. Although the correlation of Refs. [42,43] was reported to have good accuracy for general nonspherical particles, Haider's correlation seems to be the most accurate correlation for isometric particles.

In contrast to the cube, there is a lack of investigations in the open literature on the flow interaction with other angular particles, such as a tetrahedron. As one of the few works on the flow-tetrahedron interaction, Rahmani *et al.* reported that a freely settling tetrahedron has remarkably different wake vortex structures compared to a settling cube at the same Galileo number Ga and mass density ratio m. The Magnus force plays a less critical role in the lateral motion of a settling tetrahedron than in the lateral motion of a settling cube [30]. Recently, Zhang *et al.* [45] investigated and drew a new correlation for the drag coefficient $\overline{C_d}$ of the Platonic polyhedrons in the supercritical water. They reported good agreement with the available correlations for the flow past a fixed Platonic polyhedron placed with a face facing the upstream flow. However, the effects of particle angular position on the flow structures and regime transitions remain an open question. We attempt to fill the identified knowledge gap on the regime transitions of the flow past a tetrahedron, the most angular among the Platonic polyhedrons, at different angular positions, and investigate the flow past other Platonic polyhedrons in Part II of this work [46]. The current study uses a high-fidelity finite volume fictitious domain method implemented on an adaptive octree grid to perform direct numerical simulations. We explore the flow in the range of Reynolds number $100 \leqslant \mathrm{Re} \leqslant 500$ and obtain wake structures in different regimes along with force analysis.

The following is how this paper is structured: Sec. II discusses the governing equations, the numerical method, the involved dimensionless numbers, as well as the numerical setup of simulations; validations and simulation parameters are presented in Sec. III; Sec. IV discusses different flow regimes and transitions in terms of Reynolds number, the symmetry of the particle wake structures, along with an analysis on the drag, lift coefficients, the vortex shedding frequency, and the length of recirculation region; finally, the main conclusions, as well as the prospects for future work are given in Sec. V.

II. MATHEMATICAL FORMULATION AND NUMERICAL METHODS

The distributed Lagrange multiplier/fictitious domain (DLM/FD) method describes a rigid body immersed in a fluid by representing its space with a *fictitious* domain forced to behave like a rigid body. In this paper, we use the * superscript to denote dimensional quantities. Inside the cubic computational domain Ω with boundary Γ, we consider a single stationary rigid particle, i.e., an obstacle, in an incompressible fluid with density ρ_f^* and viscosity μ_f^*. We denote P as the rigid particle subdomain and $\Omega \setminus P$ the fluid subdomain to distinguish the dispersed solid phase and the carrier phase ($\Omega \setminus P \bigcap P = 0$). The main features of the fictitious domain method employed were comprehensively presented in many previous works [47–51]. Appendix A provides a summary of the main steps of the DLM/FD method, as well as details on its numerical implementation. For the sake of brevity, we do not repeat this detailed presentation here.

A. Governing equations for the fluid flow

The motion of the incompressible Newtonian fluid is governed by the Navier-Stokes equation and the continuity:

$$\rho_f^*\left(\frac{\partial \boldsymbol{u}^*}{\partial t^*} + \boldsymbol{u}^* \cdot \boldsymbol{\nabla} \boldsymbol{u}^*\right) = -\boldsymbol{\nabla} p^* + \mu_f^* \Delta \boldsymbol{u}^* \quad \text{in } \Omega \setminus P, \tag{1}$$

$$\boldsymbol{\nabla} \cdot \boldsymbol{u}^* = 0 \quad \text{in } \Omega \setminus P, \tag{2}$$

where $\boldsymbol{u}^*$ denotes the velocity vector and p^* the pressure.

We refer to the cubic computational domain boundaries (i.e., the cube faces) as left and right in the x direction, top and bottom in the y direction and front and behind in the z direction such that $\Gamma = \text{left} \cup \text{right} \cup \text{top} \cup \text{bottom} \cup \text{front} \cup \text{behind}$. $\boldsymbol{u}^*$ satisfies Dirichlet boundary conditions on the left, top, bottom, front, and behind boundaries as well as on the surface ∂P^* on the stationary particle, and homogeneous Neumann boundary conditions on the right boundary. Denoting U_0^* the inlet velocity magnitude, the complete set of boundary and initial conditions reads as follows:

$$\boldsymbol{u}^*(\boldsymbol{x}^*, t^*) = (U_0^*, 0, 0) \text{ on } \Gamma \setminus \text{right}, \tag{3}$$

$$\boldsymbol{u}^*(\boldsymbol{x}^*, t^*) = (0, 0, 0) \text{ on } \partial P, \tag{4}$$

$$\frac{\partial \boldsymbol{u}^*}{\partial x^*}(\boldsymbol{x}^*, t^*) = (0, 0, 0) \text{ on right}, \tag{5}$$

$$\boldsymbol{u}^*(\boldsymbol{x}^*, 0) = (U_0^*, 0, 0) \text{ in } \Omega \setminus P, \tag{6}$$

where $\boldsymbol{x}^* = (x^*, y^*, z^*)$ is the position vector. We also assign an arbitrary zero reference value to the pressure p^* at the right boundary.

B. Dimensionless numbers

The current study involves the following essential dimensionless quantities: (i) the particle Reynolds number Re and the particle angular position as input parameters and (ii) the drag coefficient C_d, the lift coefficient C_l and the Strouhal number St as output parameters.

The particle Reynolds number Re is defined as

$$\text{Re} = \frac{\rho_f^* U_0^* D_{\text{sph}}^*}{\mu_f^*}, \tag{7}$$

where D_{sph}^* is the equivalent volume sphere diameter, namely the diameter of a sphere which has the same volume as the tetrahedron:

$$D_{\text{sph}}^* = \left(\frac{6}{\pi} V_{\text{tetra}}^*\right)^{1/3}, \tag{8}$$

where V_{tetra}^* is the volume of the tetrahedron.

The drag coefficient C_d is defined as

$$C_d = \frac{8F_x^*}{\rho_f^* U_0^{*,2} \pi D_{\text{sph}}^{*,2}}, \tag{9}$$

where F_x^* denotes the streamwise component of the hydrodynamic force $\boldsymbol{F}^*$ exerted on the tetrahedron defined as follows:

$$\boldsymbol{F}^* = \int_{\partial P} [-p^* \boldsymbol{I} + \mu_f^* (\nabla \boldsymbol{u}^* + \nabla \boldsymbol{u}^{*,T})] \cdot \hat{n} dS = \int_P \boldsymbol{\lambda}^* d\boldsymbol{x}, \tag{10}$$

where $\hat{n}$ denotes the outward-oriented unit normal vector to the particle surface ∂P. Please note that in the context of the DLM/FD method and for a stationary particle [52], $\boldsymbol{F}^*$ is computed as the integral of the Lagrange multipliers over P in Eq. (10).

In the transverse direction, the lift coefficients can be defined similarly to the drag coefficient, as $C_{l,y}$ and $C_{l,z}$ along the y and z axis, respectively:

$$C_{l,y} = \frac{8F_y^*}{\rho_f^* U_0^{*,2} \pi D_{\text{sph}}^{*,2}}, \quad C_{l,z} = \frac{8F_z^*}{\rho_f^* U_0^{*,2} \pi D_{\text{sph}}^{*,2}}, \tag{11}$$

where F_y^* and F_z^* denote the two transverse components of the hydrodynamic force.

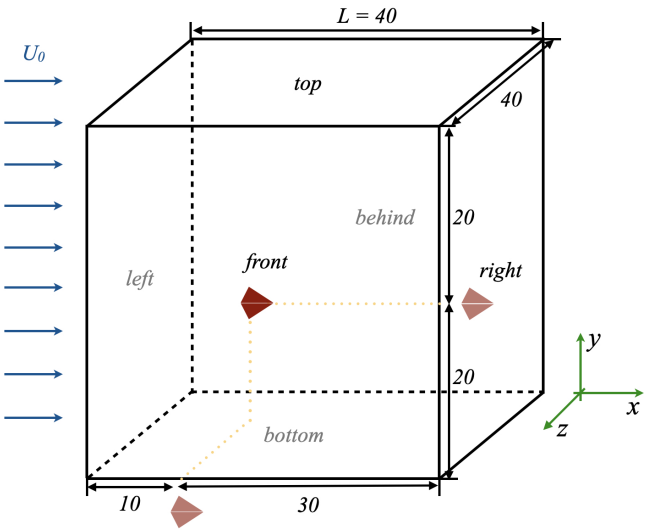

FIG. 1. Numerical setup: A fixed tetrahedron located in a cubic computational domain of side length $L = 40$, the streamwise direction is x and the flow is from left to right.

As a measurement of the fluid rotation, the three components of the dimensionless vorticity are defined by

$$\omega_x = \frac{\omega_x^* D_{\text{sph}}^*}{U_0^*}, \quad \omega_y = \frac{\omega_y^* D_{\text{sph}}^*}{U_0^*}, \quad \omega_z = \frac{\omega_z^* D_{\text{sph}}^*}{U_0^*}, \tag{12}$$

with ω_x^* (ω_y^*, ω_z^*) the corresponding component of the physical vorticity in the x (y, z) direction.

The Strouhal number describes the flow oscillating mechanism in the wake region of the particle:

$$\text{St} = \frac{f_c^* D_{\text{sph}}^*}{U_0^*}, \tag{13}$$

where f_c^* denotes the dominant frequency of the vortex shedding. Note that the Strouhal number St is therefore the dimensionless frequency using U_0^*/D_{sph}^* as the characteristic frequency scale, i.e., the inverse of the advective timescale, to make f_c^* dimensionless.

C. Numerical setup

We consider a rigid tetrahedron inside a cubic computational domain of edge length $L = L^*/D_{\text{sph}}^* = 40$. To reduce the unphysical impact of the boundaries of the finite-size computational domain on the flow-particle interaction, we need to select a large enough computational domain relative to the particle size. According to our previous work [53], the choice of $L = 40$ is deemed to be reasonable to model a flow in an unbounded domain and to avoid any major unphysical influence of the finite size of the domain on the computed solution. The Newtonian fluid enters the box and flows past a fixed tetrahedron located at $(x_p, y_p, z_p) = (10, 20, 20)$ with different angular positions as depicted in Fig. 1. The particle is centered in the two transverse y and z directions and slightly shifted to the left such that the wake flow properly develops over 30 without any artificial disturbance coming from the outflow condition on the right boundary. Such a computational domain is large enough to properly model an infinite domain of a flow at $100 \leqslant \text{Re} \leqslant 500$.

In the Cartesian octree adaptive grid strategy implemented in Basilisk, the grid refinement in the discrete regions of interest is achieved through slicing a parent cubic cell into eight subcubes [51,54]. Between two successive levels, in the hierarchical grid, the cell size differs by exactly a factor of 2. Thus, the minimal cell size of the grid ought to be $\Delta x = L/2^{n_l}$, with n_l the maximal refinement

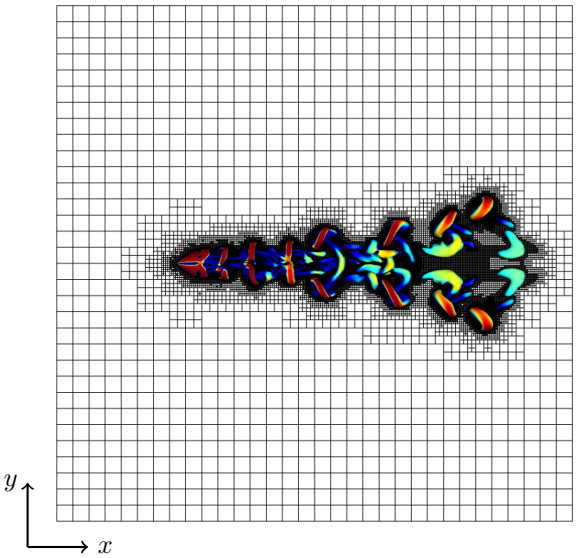

FIG. 2. Snapshot of wake structures in the early transient of the flow, identified by the isosurface of $\lambda_2 = -1$ and colored by u_x in the flow past the TE tetrahedron at Re $= 500$ with adaptive octree grid shown in the x-y plane located at $z = 20$.

level. At each time step, the Cartesian octree grid is dynamically adapted by refining the grid in regions of strong gradient variations of any field of interest. Here the primary field of interest is the flow velocity field. We also use a phase indicator field (0 in the fluid and 1 in the solid) to guarantee that the neighborhood of the particle surface is always at the finest grid resolution. Using both the velocity field and the phase indicator field for the grid adaption in Basilisk, we ensure that the flow features in both the boundary layer around the particle and the wake region are well captured. A snapshot of the Cartesian octree grid and the tetrahedron position is depicted in Fig. 2, together with the vortex structures identified by the lambda-2 isosurface [55] $\lambda_2 = -1$ in the wake region of the flow at Reynolds number Re $= 500$, colored by the magnitude of the streamwise velocity u_x. The highest level of the adaptive grid refinement (AMR) is $n_l = 12$ in Fig. 2, which guarantees enough grid points ($1/\Delta x = 102$) per equivalent diameter of the particle.

We performed a total of 120 computations, corresponding to 3 angular positions and 40 values of Re. Each computation ran on 128 cores over 12 days on average. The whole study required $128 \times 12 \times 24 \times 120 \approx 4.5$ million core-hours.

D. Particle surface points

We use a collocation point (CP) method [47,50,56] to impose the rigid body motion constraint in the particle at the discrete level on the grid. The complete set of points is the union of interior points chosen as grid nodes located inside the particle and surface points. The *parallel* point set is used to distribute the Lagrangian points as uniformly as possible on the tetrahedron surface [50]. In the parallel point set, surface points are located over lines parallel to the edges and this distribution technique also applies to other Platonic polyhedrons [53]. In the specific case of the regular tetrahedron, the faces are equilateral and the parallel point set forms the vertices of a regular equilateral triangular mesh of each face of the tetrahedron.

We illustrate the surface Lagrangian point distribution on the regular tetrahedron in Fig. 3. The uniform point-to-point distance, denoted l_{pp}, is determined by the maximal refinement level n_l and equals twice the smallest size of the grid cells $l_{\text{pp}} = 2\Delta x$. Consequently, the number of surface points grows with the refinement level n_l, providing a more accurate depiction of the particle surface.

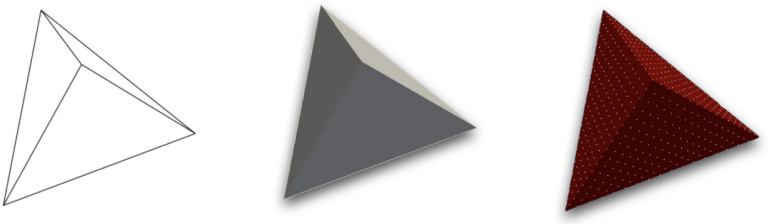

FIG. 3. Outline, surface, and Lagrangian point distribution of the tetrahedron.

E. Particle angular positions

For a tetrahedron of a given volume, we compute its edge length and its vertex coordinates in a (arbitrary but convenient) reference angular position with respect to its center of mass located at the origin of the coordinate system. We then left multiply the vertex coordinates by the appropriate rotation matrix to yield a given angular position of the tetrahedron. Finally we translate the particle with a specific angular position to $(x_p, y_p, z_p) = (10, 20, 20)$.

Denoting θ, φ and ξ the rotation angle about x, y, and z axis (right-hand rule, see Fig. 4), the corresponding rotation matrices R_x, R_y, and R_z read:

$$R_x(\theta) = \begin{bmatrix} 1 & 0 & 0 \\ 0 & \cos\theta & -\sin\theta \\ 0 & \sin\theta & \cos\theta \end{bmatrix}, \quad R_y(\varphi) = \begin{bmatrix} \cos\varphi & 0 & \sin\varphi \\ 0 & 1 & 0 \\ -\sin\varphi & 0 & \cos\varphi \end{bmatrix},$$
$$R_z(\xi) = \begin{bmatrix} \cos\xi & -\sin\xi & 0 \\ \sin\xi & \cos\xi & 0 \\ 0 & 0 & 1 \end{bmatrix}. \tag{14}$$

For a general rotation (θ, φ, ξ), the rotation matrix can be obtained by matrix multiplication:

$$\begin{aligned} R(\theta, \varphi, \xi) &= R_x(\theta) \cdot R_y(\varphi) \cdot R_z(\xi) \\ &= \begin{bmatrix} \cos\theta\cos\varphi & \cos\theta\sin\varphi\sin\xi - \sin\theta\cos\xi & \cos\theta\sin\varphi\cos\gamma + \sin\theta\sin\xi \\ \sin\theta\cos\varphi & \sin\theta\sin\varphi\sin\xi - \cos\theta\cos\xi & \sin\theta\sin\varphi\cos\gamma + \cos\theta\sin\xi \\ -\sin\varphi & \cos\varphi\sin\xi & \cos\varphi\cos\xi \end{bmatrix}. \end{aligned} \tag{15}$$

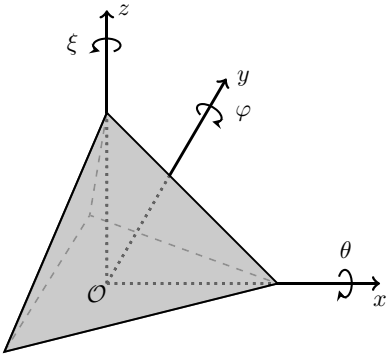

FIG. 4. Definition of rotation angles θ, φ, and ξ with respect to the three coordinate axes.

Particle	E/F/V	3D view	Edges	Proj.	$S_{pp,x}$
Tetrahedron	TE		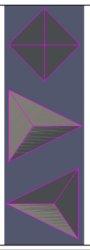		1.721
	TF				1.490
	TV				1.490

FIG. 5. Geometric features in the y-z plane of the tetrahedron in its three angular positions: 3D view, projection of edges (Edges), projection of outline (Proj.), and crosswise cross-sectional surface area ratio $S_{\mathrm{pp},x} = S^*_{\mathrm{pp},x}/S^*_{\mathrm{sph}}$.

Using the rotation matrix (θ, φ, ξ), we explore the three following specific angular positions of the tetrahedron: face facing the flow (TF), edge facing the flow (TE), and vertex facing the flow (TV). For simplicity, a complete listing of the coordinates of the tetrahedron vertices with respect to its mass center is given in Table V of Appendix B.

Figure 5 lists the tetrahedron geometric features along the streamwise direction (x^+-direction, in the y-z plane). A 3D image in the y-z plane depicts the front surface of the tetrahedron as *seen* by the incoming fluid flow. The edges of the tetrahedron are highlighted as pink lines in the fourth column (Edges) of Fig. 5. A projected view (Proj.) reveals the outline of the tetrahedron and the crosswise cross-section. The surface area of the crosswise cross-section is denoted $S^*_{\mathrm{pp},x}$. The last column gives the ratio $S_{\mathrm{pp},x}$ of the particle crosswise cross-sectional surface area of the tetrahedron $S^*_{\mathrm{pp},x}$ to that of the volume-equivalent sphere $S^*_{\mathrm{sph}} = \pi D^{*,2}_{\mathrm{sph}}/4$. $S_{\mathrm{pp},x}$ of the edge facing the flow tetrahedron (TE) is found to be larger than that in the other two angular positions, while $S_{\mathrm{pp},x}$ of the face facing the flow tetrahedron (TF) and $S_{\mathrm{pp},x}$ of the vertex facing the flow tetrahedron (TV) are equal.

The side views of the tetrahedron at the three angular positions (TE, TF, TV) are shown in Fig. 6. We show the outline of the projected tetrahedron in the x-z and the x-y planes. We also provide the ratio of the tetrahedron lateral cross-sectional surface area to that of the volume-equivalent sphere in the y direction, denoted $S_{\mathrm{pp},y}$ and in the z direction, denoted $S_{\mathrm{pp},z}$. The lateral cross-sectional surface area $S_{\mathrm{pp},y}$ of the tetrahedron along the y axis (x-z plane) is almost identical (difference less than 0.1%) at the three angular positions. Along the z axis (x-y plane), the lateral cross-sectional surface area $S_{\mathrm{pp},z}$ changes slightly more. Figures 5 and 6 provide a clear visualization of the three orthogonal projections of the tetrahedron (TE, TF, TV) and help to comprehend the three-dimensional flow-particle interaction.

Particle	E/F/V	$x-z$ view	$S_{pp,y}$	$x-y$ view	$S_{pp,z}$
Tetrahedron	TE		1.217		1.217
	TF		1.217		1.405
	TV		1.217		1.405

FIG. 6. Geometric features in the x-z and x-y planes of the tetrahedron in its three angular positions: projection of outline and lateral cross-sectional surface area ratios $S_{\mathrm{pp},y} = S^*_{\mathrm{pp},y}/S^*_{\mathrm{sph}}$, $S_{\mathrm{pp},z} = S^*_{\mathrm{pp},z}/S^*_{\mathrm{sph}}$.

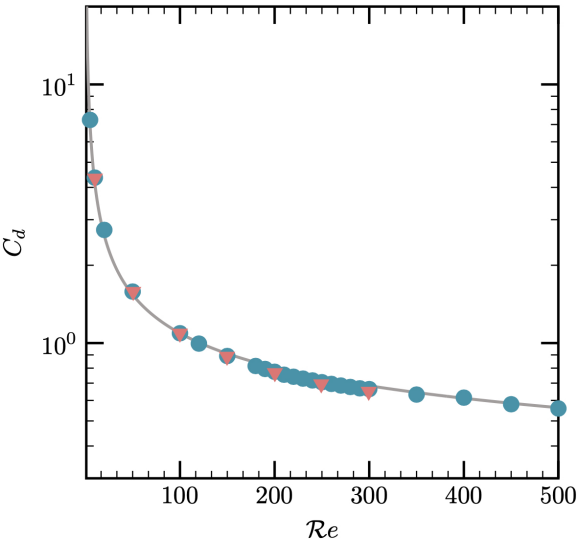

FIG. 7. Time-time-averaged drag coefficient $\overline{C_d}$ as a function of Re in the flow past a fixed sphere at $1 \leqslant \mathrm{Re} \leqslant 500$ (●), comparison with numerical results of Selçuk *et al.* [51] (▼) and the Schiller-Naumann correlation (——).

III. VALIDATIONS

A. Flow past an obstacle

We first perform computations of the flow past a fixed isolated sphere at small and moderate Reynolds numbers $1 \leqslant \mathrm{Re} \leqslant 500$. We plot in Fig. 7 the evolution of the time-averaged drag coefficient $\overline{C_d}$ of the sphere as a function of Reynolds number Re. In agreement with the large body of work in the literature, see, e.g., Refs. [14,51], the drag coefficient $\overline{C_d}$ decreases with Re. Please note that the results from [51] were obtained with the same DLM/FD method but with a slightly different numerical setup. Overall, we obtain a very satisfactory agreement between our computed results and results in the literature. The maximum relative error with respect to the Naumann-Schiller correlation is less than 3% in the range $1 \leqslant \mathrm{Re} \leqslant 500$. This confirms prior validations from [51,53], the reliability of our numerical method and its implementation in Basilisk.

The particle wake flow structures are identified by the lambda-2 isosurface [55] $\lambda_2 = -1$, as shown in Fig. 8. In Figure 8(a), $\mathrm{Re} = 210$ and the flow is in the axisymmetric regime without any vortex formed in the wake region. When Re increases to 220, as shown in Fig. 8(b), two long leglike

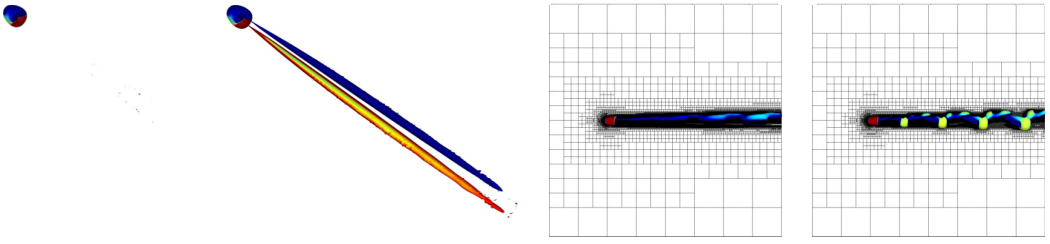

(a) (b) (c) (d)

FIG. 8. Wake structures identified by the isosurface of $\lambda_2 = -1$ and colored by u_x in the flow past a fixed sphere: (a) axisymmetric regime ($\mathrm{Re} = 210$), (b) beginning of planar-symmetric regime ($\mathrm{Re} = 220$), (c) end of planar-symmetric regime ($\mathrm{Re} = 270$), and (d) periodic hairpin vortex shedding regime ($\mathrm{Re} = 280$).

TABLE I. Comparison of $\overline{C_d}$ if the flow at different Re past a TF tetrahedron. Note that $\overline{C_d}$ at the same Re are highlighted in the same color.

Code	(L_x, L_y, L_z)	$\mathcal{R}e$	$1/\Delta x$	$\overline{C_d}$
This work	(24, 24, 24)	10	85	5.87
This work	(24, 24, 24)	50	85	2.46
This work	(24, 24, 24)	100	85	1.92
PeliGRIFF	(24, 16, 16)	10	40	5.92
PeliGRIFF	(24, 16, 16)	50	40	2.50
PeliGRIFF	(24, 16, 16)	100	60	1.94

tails appear as reported in the work of Ref. [14]. Our results therefore reproduce well the transition of the flow past a sphere from axisymmetric to planar symmetric regime when $210 < \mathrm{Re} < 220$. We observe a second transition when the Reynolds number increases from $\mathrm{Re} = 270$ to $\mathrm{Re} = 280$. The two long leglike tails begin to fluctuate, and our results feature hairpin vortex shedding at $\mathrm{Re} = 280$, as shown in Figs. 8(c) and 8(d). Thus, we capture well the transition to the vortex shedding regime that happens at a Re between 270 and 280. These two transitions in Fig. 8 are well documented in the literature and in particular were confirmed by the experimental work of Klotz *et al.* [20]. The case of the flow past a sphere validates the robustness of our numerical code and provides reference values for the grid refinement settings.

As a second validation step, we perform computations of the steady flow past a face facing the flow tetrahedron (TF) at different Reynolds numbers $\mathrm{Re} = 10, 50, 100$. Table I shows the comparison of results computed by the present DLM/FD numerical method implemented on octree grids to results computed by PeliGRIFF (parallel efficient library for GRains in fluid flow), our legacy code that features a DLM/FD method implemented on regular fixed Cartesian grids [49,50]. Table I provides the dimensionless size of the computational domain (L_x, L_y, L_z) and the corresponding number of smallest grid cells per volume-equivalent sphere diameter $1/\Delta x$. The tetrahedron is discretized with at least 40 (in the PeliGRIFF simulations at $\mathrm{Re} = 10$ and $\mathrm{Re} = 50$) grid cells per D^*_{sph} and this relatively coarse grid resolution is deemed to supply an accurate enough solution for the purpose of validation.

We find an excellent agreement between the two solvers using two different types of grid. The relative errors for $\overline{C_d}$ of the flow at $\mathrm{Re} = 10$ ( ), $\mathrm{Re} = 50$ ( ), and $\mathrm{Re} = 100$ ( ) are 0.84%, 1.6%, and 1.03%, respectively. We reasonably speculate that with a higher spatial resolution in the regular fixed Cartesian grid computations in PeliGRIFF, the relative errors would be even smaller. The small discrepancy may also be attributed to a slightly different transverse size of the computational domain (16 versus 24, see Table I), at least at the lowest $\mathrm{Re} = 10$, without being really significant. Consequently, we have sufficient confidence to accurately compute and analyze the more challenging problem of the flow past a tetrahedron at higher Re. The adaptive mesh refinement (AMR) of octree grids saves a tremendous amount of computational resources at higher Re compared to a regular fixed Cartesian grid with the same spatial resolution.

B. Grid and time resolution

1. Grid resolution

In this section, we choose the smallest grid resolution Δx to properly capture the flow structures in the flow domain especially for the unsteady flows at high Re. We select the *pyramid* configuration (depicted in Fig. 4, dimensionless vertex coordinates given in Table V) at $\mathrm{Re} = 300$ and perform a series of computations with an increasing maximum level of refinement $8 \leqslant n_l \leqslant 12$. The Cartesian octree grid in Basilisk provides a practical and efficient arrangement for dynamic grid refining and coarsening in particular in the particle boundary layer and the wake region. The Cartesian octree grid is more efficient than the classical multigrid technique and its uniform spatial resolution [57]. In the

TABLE II. Spatial convergence of $\overline{C_d}$ with grid refinement. L denotes the domain size normalized by equivalent diameter, n_l the adaptive grid refinement level, N_{cell} the total number of cells, and $1/\Delta x$ number of cells per equivalent diameter.

L	n_l	N_{cell}	$1/\Delta x$	$\overline{C_d}$
40	8	1.95×10^5	6	2.295
40	9	7.45×10^5	12	1.887
40	10	3.16×10^6	25	1.662
40	11	1.17×10^7	51	1.624
40	12	3.24×10^7	102	1.578

computational domain, the Cartesian octree grid features a variable resolution, with the maximum level of refinement denoted n_l and the smallest grid size determined by: $\Delta x = L/2^{n_l}$.

We report $\overline{C_d}$ as a function of the grid refinement level n_l in Table II. We also provide the corresponding smallest grid resolution in terms of the number of points per equivalent diameter $1/\Delta x$ and the total number of cells in the computational domain N_{cell}. On a uniform grid, N_{cell} would be multiplied by 8 when the grid size Δx is divided by 2. This is not the case for a Cartesian octree grid that features variable grid resolution in the flow and dynamically refines the grid in the region of interest. Thus, N_{cell} increases at a much lower rate than in a uniform grid. With n_l increasing from 8 to 12 (total number of cells from 1.95×10^5 to 3.24×10^7), $\overline{C_d}$ decreases monotonically. From $n_l = 11$ ($1/\Delta x = 51$), $\overline{C_d}$ does not vary much with Δx and the drag coefficient $\overline{C_d}$ converges smoothly to the value 1.578 at $n_l = 12$.

To get a more quantitative picture of grid resolution convergence, we fit the drag coefficient $\overline{C_d}$ data in Table II with a function of the form $C_{d,\text{ref}} + \alpha \Delta x^{n_p}$. The intercept $C_{d,\text{ref}}$, the slope α and the power n_p are determined by nonlinear regression. The best fitting curve for the data comes with $\alpha \approx 7.18$ and $n_p \approx 1.22$. Figure 9(a) shows a solid linear correlation between $\overline{C_d}$ and $\Delta x^{1.22}$ with a coefficient of determination $R^2 = 0.997$. Subsequently, we take the intercept of the linear fitting curve with the y axis as the reference value of the drag coefficient, and obtain $C_{d,\text{ref}} \approx 1.55$. Alternatively, we can present results in terms of the (relative) error with respect to the reference

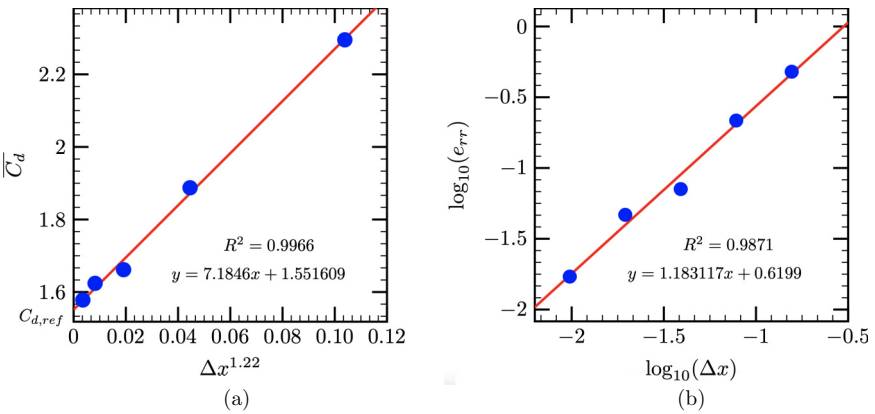

FIG. 9. Spatial convergence of $\overline{C_d}$ as a function of the minimal grid size Δx for the flow past a pyramid tetrahedron: simulation results (●) and fitting curve (—).

value $C_{d,\mathrm{ref}} \approx 1.55$ defined as

$$e_{\mathrm{rr}} = \frac{|\overline{C_d} - C_{d,\mathrm{ref}}|}{C_{d,\mathrm{ref}}}. \tag{16}$$

Assuming that e_{rr} has the form of a power function $\tilde{\alpha}\Delta x^{\widetilde{n_p}}$, we deduce the convergence rate $\widetilde{n_p}$ through linear regression of $\log_{10}(e_{\mathrm{rr}})$ versus $\log_{10}(\Delta x)$ as shown in Fig. 9(b). Ideally, we should get $n_p = \widetilde{n_p}$ but the best fitting curve in Fig. 9(b) only gives $n_p \simeq \widetilde{n_p}$. Considering that the former regression is nonlinear using the original data set while the latter is a linear regression of $\log_{10}$-transformed data, the two values $n_p = 1.22$ and $\widetilde{n_p} = 1.18$ are deemed to be close enough.

Consequently, our numerical results converge well with increasing grid resolution and the order of convergence lies between 1.1 and 1.3, in line with earlier findings [50,53]. We also confirm that selecting $n_l = 12$ as the maximum level of refinement with a corresponding smallest grid resolution of $1/\Delta x = 102$ delivers satisfactory results that are almost insensitive to further grid refinement. Therefore, we safely use ($n_l = 12, 1/\Delta x = 102$) for all computations in the work. The generated data set with such a spatial resolution is now physically analyzed in a reliable manner exempt from major biases stemming from spatial errors in the computations.

2. Time resolution

We choose the advective timescale $t^*_{\mathrm{ref}} = D^*_{\mathrm{sph}}/U^*_0$ as the characteristic timescale. In all our simulations, the time step $\Delta t = \Delta t^*/t^*_{\mathrm{ref}}$ is selected to satisfy the two following constraints:

(1) the dimensionless time step Δt is bounded by 10^{-3} to make the operator splitting error negligible;

(2) the Courant-Friedrich-Levy condition is satisfied to guarantee the numerical stability of the explicit treatment of the advection term in the momentum conservation equation.

In the mathematical form, the time step Δt is dynamically updated at each discrete time by

$$\Delta t = \min\left\{10^{-3}, \min_m \frac{0.8\Delta x_m}{|\boldsymbol{u}_m|}\right\}, \tag{17}$$

where m is an index spanning all grid cells. Most of our simulations run up to at least $t = t^*/t^*_{\mathrm{ref}} = 300$. Some cases run up to $t = 800$, especially for $150 \leqslant \mathrm{Re} \leqslant 200$ when the lift coefficients rise and the flow takes a long time to become unsteady. Computing the flow over such long physical times guarantees the complete establishment of the flow regimes and enables us to perform a reliable statistical analysis of the time behavior of the flow in unsteady cases.

IV. RESULTS

A. Flow regime transition

We discuss the regime transitions of the flow past a fixed tetrahedron at three angular positions (TE, TF, TV) with 41 different Re in the range of $100 \leqslant \mathrm{Re} \leqslant 500$. Table III shows the comprehensive regime map as a function of the Reynolds number Re for the three angular positions of the tetrahedron. The flow regimes are determined by different aspects of the wake structure using the λ_2 criterion, vorticity and vortex shedding frequency. Cases in the same regime are highlighted in the same color. Starting from a steady regime at relatively low Re, the flow past a tetrahedron turns unsteady and starts a hairpin vortex shedding regime before the wake region becomes chaotic at higher Re. The critical Reynolds numbers $\mathrm{Re}_{\mathrm{cr}}$ for regime transitions vary with the angular position of the tetrahedron.

In the TE case, we find a new symmetric double-hairpin vortex shedding regime (DHS) that begins at $\mathrm{Re} = 190$. Unlike the regime transitions of a sphere or a cube, the double-hairpin vortex shedding appears before the breakup of the planar symmetry in the wake region. For $190 \leqslant \mathrm{Re} \leqslant 280$, the double-hairpin vortex shedding (DHS-I) keeps a *quasi*orthogonal symmetry with respect to both the x-y plane and the x-z plane. With increasing Re, the vortex structure symmetry with

TABLE III. Regime map of the flow past a tetrahedron at the three angular positions (A.P.): multiaxis steady symmetry ( ), planar steady symmetry ( ), periodic vortex shedding ( ), and chaotic vortex shedding ( ).

A.P.	Regime I	Regime II	Regime III	Regime IV
TE	$100 \leq \mathcal{R}e \leq 180$ Orthogonal steady-symmetry (OSS)	$190 \leq \mathcal{R}e \leq 330$ Double-hairpin vortex shedding (DHS-I)	$340 \leq \mathcal{R}e \leq 360$ Double-hairpin vortex shedding (DHS-II)	$370 \leq \mathcal{R}e \leq 500$ Chaotic shedding (CS)
TF	$100 \leq \mathcal{R}e \leq 120$ Tri-axis steady-symmetry (TSS)	$130 \leq \mathcal{R}e \leq 140$ Planar steady-symmetry (PSS)	$150 \leq \mathcal{R}e \leq 230$ Hairpin vortex shedding (HS)	$240 \leq \mathcal{R}e \leq 500$ Chaotic shedding (CS)
TV	$100 \leq \mathcal{R}e \leq 150$ Tri-axis steady-symmetry (TSS)	$160 \leq \mathcal{R}e \leq 180$ Planar steady-symmetry (PSS)	$190 \leq \mathcal{R}e \leq 260$ Hairpin vortex shedding (HS)	$270 \leq \mathcal{R}e \leq 500$ Chaotic shedding (CS)

respect to the x-z plane breaks down and keeps a planar symmetry with respect to the x-y plane at $290 \leqslant \mathrm{Re} \leqslant 330$. We notice that the planar symmetric structure becomes broken and unsteady from $\mathrm{Re} = 340$. The double-hairpin vortex structure persists in the range $340 \leqslant \mathrm{Re} \leqslant 360$ and we denote it DHS-II regime in Table III. Once the symmetry of the wake structure breaks down, we observe a quick transition from the DHS regime to a chaotic vortex shedding regime (CS) at $\mathrm{Re} = 370$.

In the TF case, the triplanar steady symmetry (TSS) breaks at a relatively low $\mathrm{Re} = 130$. After a short range of Re where the wake shows planar steady symmetry (PSS), the hairpin vortex shedding (HS) begins at $\mathrm{Re} = 150$. Note that the flow still remains steady (OSS) at $\mathrm{Re} = 150$ in the TE case. This clearly shows the effects of the angular position on regime transitions. Finally, the chaotic vortex shedding (CS) starts from $\mathrm{Re} = 240$. The TV case exhibits a similar sequence of regimes as the TF case, except that the $\mathrm{Re}_{\mathrm{cr}}$ are all slightly higher. We take a closer look at these regimes in the following discussion.

B. Vorticity and wake symmetry

The regime transitions can be well depicted by the three components of the vorticity ω in the y-z plane. Figures 10–12 all show the vorticity distribution in the wake region of the tetrahedron

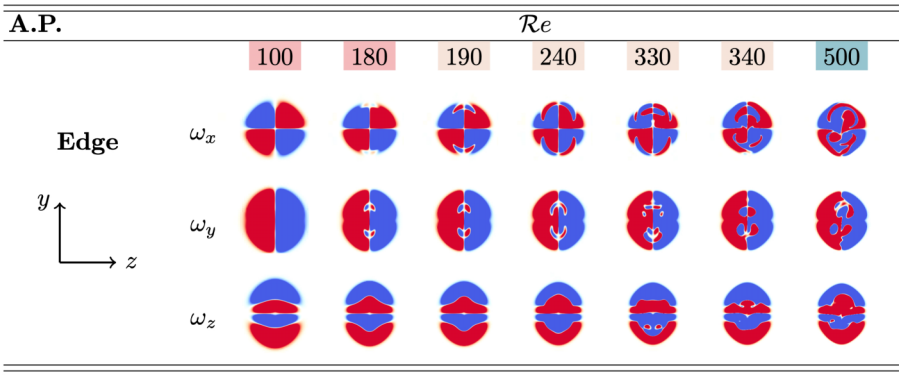

FIG. 10. Symmetry of the vortex structure (identified by ω_x, ω_y, and ω_z, positive in red, negative in blue, and near-zero in white) in the wake region of the TE tetrahedron in the y-z plane located at $x = x_p + 1.5$.

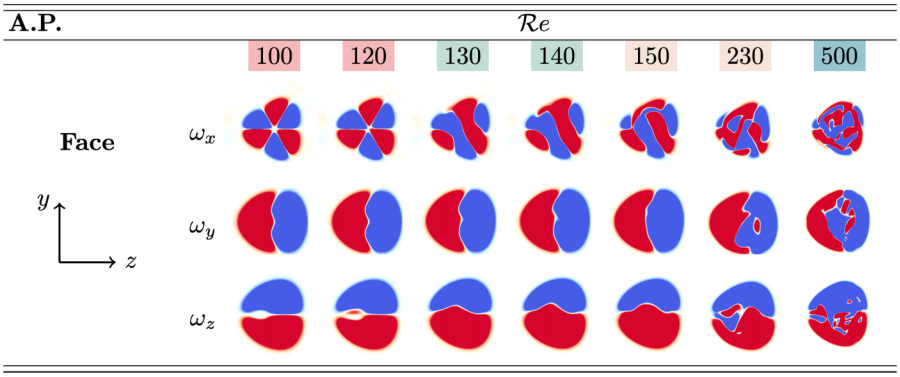

FIG. 11. Symmetry of the vortex structure (identified by ω_x, ω_y, and ω_z, positive in red, negative in blue, and near-zero in white) in the wake region of the TF tetrahedron in the y-z plane located at $x = x_p + 1.5$.

in the y-z plane at $x = x_p + 1.5$ (the vorticity distribution is consistent and can also be discerned at a larger distance in the wake) and depicts the flow structure evolution with increasing Re. Please note that in the cases where the flow is unsteady, the vorticity distribution shown in the aforementioned figures corresponds to a snapshot at a time when the flow regime is established. In the DHS regime, we choose instantaneous fields that distinctly exhibit the double-hairpin structure. In the chaotic regime, we randomly select a time that properly illustrates the chaotic nature of the wake structures. To highlight the vortex structures, we observe that the spatial average of all components of ω is approximately 0 at any time. Consequently, we plot in Fig. 10 in red regions where $\omega_{i,\max}/100 \leqslant \omega_i \leqslant \omega_{i,\max}$, $i = x, y, z$ where $\omega_{i,\max} > 0$ is the maximum value of ω_i, in blue regions where $\omega_{i,\min} \leqslant \omega_i \leqslant \omega_{i,\min}/100$, $i = x, y, z$, where $\omega_{i,\min} < 0$ is the minimum value of ω_i. Regions in white therefore correspond to the narrow range $\omega_{i,\min}/100 \leqslant \omega_i \leqslant \omega_{i,\max}/100$ where we can consider that $\omega_i \approx 0$.

We present the distribution of the vorticity components in the wake region of a TE tetrahedron at different Re in Fig. 10. All three vorticity components exhibit a symmetric pattern at low Re, e.g., at Re $= 100$. The streamwise component of the vorticity ω_x exhibits an orthogonal symmetric pattern with respect to the y axis and the z axis, which is similar to the orthogonal steady symmetry regime (OSS) of the flow past a fixed cube [35]. The transverse component ω_z has a sandwich pattern, where the positive and negative layers of ω_z appear alternatively and remain symmetric to the z axis. Similarly, the ω_y remains symmetric to the y axis in the steady flow regimes. With increasing Re, the hairpin vortex shedding appears at $180 <$ Re < 190, as shown by the streamwise

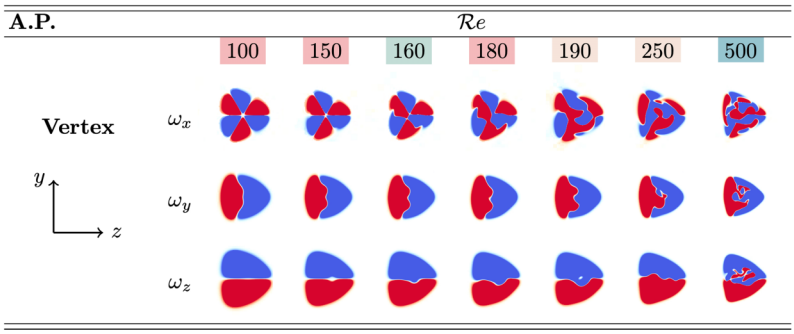

FIG. 12. Symmetry of the vortex structure (identified by ω_x, ω_y, and ω_z, positive in red, negative in blue, and near-zero in white) in the wake region of the TV tetrahedron in the y-z plane located at $x = x_p + 1.5$.

component of the vorticity ω_x. At Re = 180, the wake flow structure is steady and orthogonal-symmetric. Then, we can see two crescent moon structures emerging from the two rear corners of the edge tetrahedron as shown in ω_x at Re = 190. We remind the readers that the rear edge of TE is parallel to the y axis as shown in Fig. 5. As a direct consequence of the hairpin vortex shedding, these small crescents, or the legs of the hairpin vortices, move periodically along the y axis. The crescent structure length increases with Re. In the first stage of the DHS-I regime, the flow structures in the TE wake region are *quasi*orthogonal symmetric. The length of the crescent vortex pairs on the opposite sides of the z axis is slightly different at some specific times and then again almost equal at some other times. Thus, this orthogonal symmetry is not *perfect* but still remarkable. Then in the second stage of the DHS-I regime, the symmetry with respect to the z axis becomes slightly degenerated and the vortex structure in ω is symmetric with respect to the y axis only at $290 \leqslant \mathrm{Re} \leqslant 330$ in Fig. 10. At Re = 340, we see that the vortex structure in ω fluctuates spatially and the planar symmetry starts to break down while keeping the double-hairpin vortex structure (DHS-II). The flow past the TE tetrahedron transitions from the double-hairpin vortex shedding (DHS) to the chaotic vortex shedding (CS) when Re reaches 370. The periodic shedding ends and the temporal evolution of the ω_x flow structure in the y-z plane develops a visible unorganized and chaotic pattern. Compared to the streamwise component ω_x, the transverse components ω_y and ω_z seem to show less information about the vortex structures in the steady regime. For example, we can only observe a planar symmetric pattern on the ω_y and ω_z plots at Re = 100. Since there are no hairpin structures in ω_z, the transition from OSS to DHS cannot be elucidated on the ω_z plot from Re = 180 to Re = 190. These two parameters are however good markers of the transition from the DHS regime to the CS regime as they also lose their planar symmetry over this transition.

We present the distribution of the vorticity components in the wake region of a TF tetrahedron at different Re in Fig. 11. In the steady regime, e.g., Re = 100, the vorticity components are all symmetric with respect to the z axis and ω_x shows a triaxis symmetric pattern where a pair of opposite-signed vortices ω_x originate from each edge of the tetrahedron front surface, leading to six *petals* of the same size. With the increase of Re, the ω_x triaxis symmetry breaks down to a *single-axis* symmetry (or single planar symmetry in three dimensions) as shown at Re = 130. Then for Re > 150, the planar steady symmetry (PSS) regime transitions to a single-hairpin vortex shedding (HS) regime. The hairpin vortices behind the TF tetrahedron originate from the rear corner. The interval of Re over which HS occurs is relatively narrow compared to the TE case. Starting from Re = 240, the vortex shedding becomes chaotic.

We present the distribution of the vorticity components in the wake region of the TV tetrahedron at different Re in Fig. 12. While the TV tetrahedron opposes a different front surface geometry to the flow than that opposed by the TF tetrahedron, the TV tetrahedron exhibits vortex structures that resemble those of the TF tetrahedron in the particle wake region. Similar to what we observed in the other two angular positions (TE, TF), the streamwise vorticity component ω_x provides more details about the wake structure symmetry and regime transitions in the flow past a TV tetrahedron. The steady triaxis symmetry regime exists until Re = 150, and then some small structures appear on the rim of the ω_x plot while keeping a planar symmetry at Re = 160. The HS regime begins at Re = 190 and the shedding originates from the center of the rear face of the TV tetrahedron. Please note that the planar symmetry in the particle wake region breaks down immediately after the onset of the hairpin vortex shedding in the TF and TV cases (e.g., Re = 150 in Fig. 11 and Re = 190 in Fig. 12). Finally at Re = 270, the CS regime takes place. An example of the vorticity components in the CS regime is given for the flow at Re = 500.

Figure 13 presents three-dimensional side views of the streamwise vorticity ω_x as a function of Re in the form of isosurfaces of $\omega_x = \pm 0.03$ for the three angular positions of the tetrahedron. The regime transitions with increasing Re discussed in the above are visually further emphasized. In the steady regime, the TE tetrahedron has four opposite-signed vortex tails in the wake region originating from the tetrahedron front edge. With increasing Re, all tails grow longer until Re = 180 when we start to notice some small periodic fluctuations on the long tail surfaces. From Re = 190 in the DHS-I regime, periodic vortices start shedding in the particle wake region. In Fig. 13(a), the

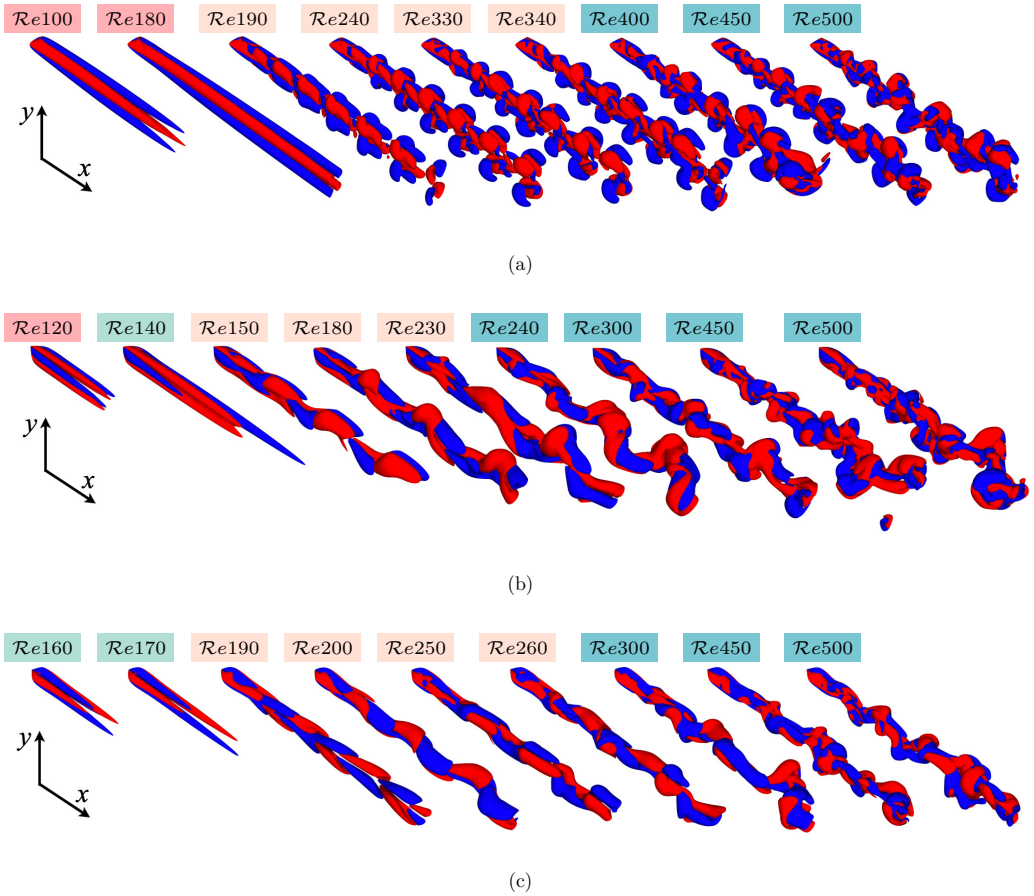

FIG. 13. Side view of the wake structures identified by the isosurfaces $\omega_x = \pm 0.03$ as a function of Re. (a) TE tetrahedron, (b) TF tetrahedron, and TV tetrahedron.

alternately shed vortices have the shape of small *mushrooms* instead of *hairpins*. We see that these mushroom vortices remain symmetric with respect to the y axis from Re $= 240$ to Re $= 330$ and then spatially fluctuate in the far wake at Re $= 340$, indicating the onset of the DHS-II regime. These vortex structures were already observed in two dimensions in Fig. 10 in the y-z plane behind the tetrahedron. For Re > 370, the vortex structures progressively stretch when they move farther and farther away from the particle in the wake.

For the TF and TV tetrahedrons, we notice six tails in the wake region of the particle in the multiaxis steady regime. The three pairs of opposite-signed vortex tails originate from the three front edges of the tetrahedron (the three edges of the front face perpendicular to the flow in the TF case and the three edges originating from the front tip in the TV case), which are bundled, relatively thin and short compared to that of the TE tetrahedron. Hence, they are more sensitive to flow fluctuations and their length becomes uneven when Re increases. The HS regime begins and exhibits periodic alternate vortex shedding in the particle wake at Re $= 150$ for the TF tetrahedron and at Re $= 190$ for the TV tetrahedron. The alternately shed vortices are intertwined and mixed up during the periodic shedding starting from Re $= 180$ for the TF tetrahedron. We notice that the vortex structures in the TV case are slimmer than that in the TF case. The periodic alternate vortex shedding is still observed at Re $= 250$ in the TV case. Then the vortex structures eventually become intertwined as well. In both the TF and TV cases, the angular position in the y-z plane of the shedding

plane that always contains the x axis and splits the wake into alternating vortices depends on Re and also slightly oscillates in time around an average angular position. We get a glimpse of this variable angular position of the shedding plane by comparing Re = 180 and Re = 240 in Fig. 13(b) and Re = 200 and Re = 260 in Fig. 13(c), where the shedding planes are clearly different in the same HS regime. The oscillation of the vortex shedding plane directly impacts the transverse force time evolution. Once the HS regime ends at higher Re, the vortex structures become chaotic.

Generally, vorticity isosurfaces are a suitable tool to visualize the flow structures in the tetrahedron wake region. The streamwise component is clearly able to elucidate the symmetry of the wake region and the regime transition from steady to unsteady flows. It is less efficient in explaining the vortex shedding structures, that can be better understood using the λ_2 criterion.

C. Loss of stationarity and vortex shedding

Figure 14 presents the evolution of the vortex structures identified by the isosurface $\lambda_2 = -1$ in the flow past the TE tetrahedron at different Re. The flow structures are shown in three dimensions but the view is perpendicular to the x-z plane on the left half and to the $x - y$ plane on the right half in Fig. 14. Similar to the ω_x isosurfaces, the steady flow at low Re = 140 features four straight vortex tails of the same length in the particle wake region. At Re = 180, some small amplitude spatial oscillations appear on the vortex tails in the far-wake region, but the flow remains steady. Then, a clear symmetric DHS pattern manifests in the x-y plane at Re = 190. The unique form of the DHS is due to the same relative angle between the two faces forming the front surface and the two faces forming the rear surface of the TE tetrahedron. First separated by the two front faces, the fluid flow is guided to converge smoothly by the two rear faces. The streamlines are stretched at a minimal level and thus keep a high level of symmetry in the wake region. Double-hairpin vortices are generated simultaneously from the two rear corners of the TE tetrahedron, as depicted in the x-y plane of Fig. 14.

Three remarkable features are noticed for the double-hairpin vortex shedding (DHS-I and DHS-II) regime:

(1) The double-hairpin vortex presents a high level of symmetry in an unsteady flow. Considering Re = 240 as an illustrative example, we see that the double-hairpin vortices have a *quasi*orthogonal symmetry with respect to the y and z axis. Then, the double vortices become slightly staggered in the x-y plane at Re = 330 but still keep a planar symmetry in the x-z plane with respect to the y axis.

(2) Compared to the single vortex shedding in the wake region of a sphere, a cube or the tetrahedron at the other two angular positions (TF, TV), the dominant frequency of DHS is almost twice. We see from Fig. 14 that the shedding frequency does not change significantly throughout the DHS regime.

(3) The hairpin legs always have a leading position compared to the hairpin heads which makes the double-hairpin structure inverse to the single hairpin structure. A clear comparison can be found in Figs. 14 and 16. The span of the double-hairpin vortex in the x-y plane is almost twice as large as that in the x-z plane. We observe a *flat* vortex shedding mode in the TE case, although the tetrahedron is a perfectly *isometric* angular particle.

At Re = 340, the double-hairpin vortex loses its planar symmetry in the x-y plane and the lift coefficient C_l starts increasing in the DHS-II regime. For larger Re $>$ 370, the flow regime becomes chaotic and we notice the entanglement of the coherent structures but the trace of the double-hairpin vortices is still partially observable.

Figures 15 and 16 present the wake structures identified by the isosurface $\lambda_2 = -1$ in the TF case and in the TV case, respectively. At low Re $<$ 150, the λ_2 criterion shows some vortex fragments in the wake region. Please note that these two angular positions of the tetrahedron break the orthogonal symmetry of the flow and thus lead to a nonzero lift force even in the low Re steady regime. The lengths of the vortex tails become uneven at Re = 130 in the TF case and at Re = 160 in the TV case. Correspondingly, the lift coefficient further increases due to the contribution of these vortex

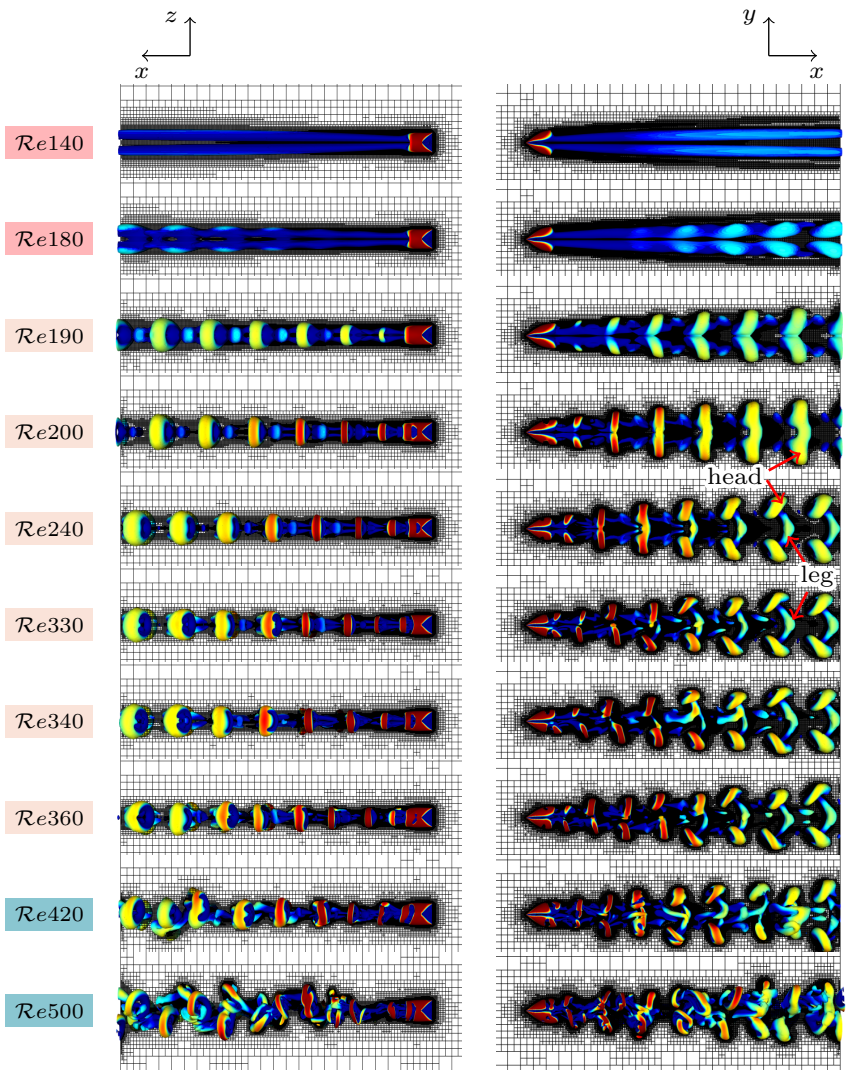

FIG. 14. Wake structures of the flow past a TE, colored by u_x (low velocity in blue and high velocity in red), as a function of Re, identified by the isosurface $\lambda_2 = -1$; views in the x-z plane (left) and the x-y plane (right).

tails. From Figs. 15 and 16, the hairpin vortices originate from the rear vertex in the TF case and from the center of the rear face in the TV case. The HS regime exists only for a relatively narrow interval of $150 \leqslant \mathrm{Re} \leqslant 230$ in the TF case and a very typical hairpin shedding is depicted at $\mathrm{Re} = 180$ in Fig. 15. We see that the hairpin head stays in front of the hairpin legs in the wake, similar to the flow past a fixe cube or sphere. Three periods of the vortex shedding are visible at $\mathrm{Re} = 180$ within a length of 30 downstream of the TF tetrahedron in Fig. 15 versus six periods in the TE case at $\mathrm{Re} = 240$ in Fig. 14. The HS regime in the TV case features many similarities with the TF case as illustrated in Fig. 16, namely similar single-hairpin vortex shedding, comparable shedding frequency and analogous vortex structures. The single hairpin vortex structure appears to be slightly slimmer in the TV case than in the TF case, as also observable in Fig. 13, although this difference is not significant. One plausible explanation is that the recirculation region behind the TV tetrahedron

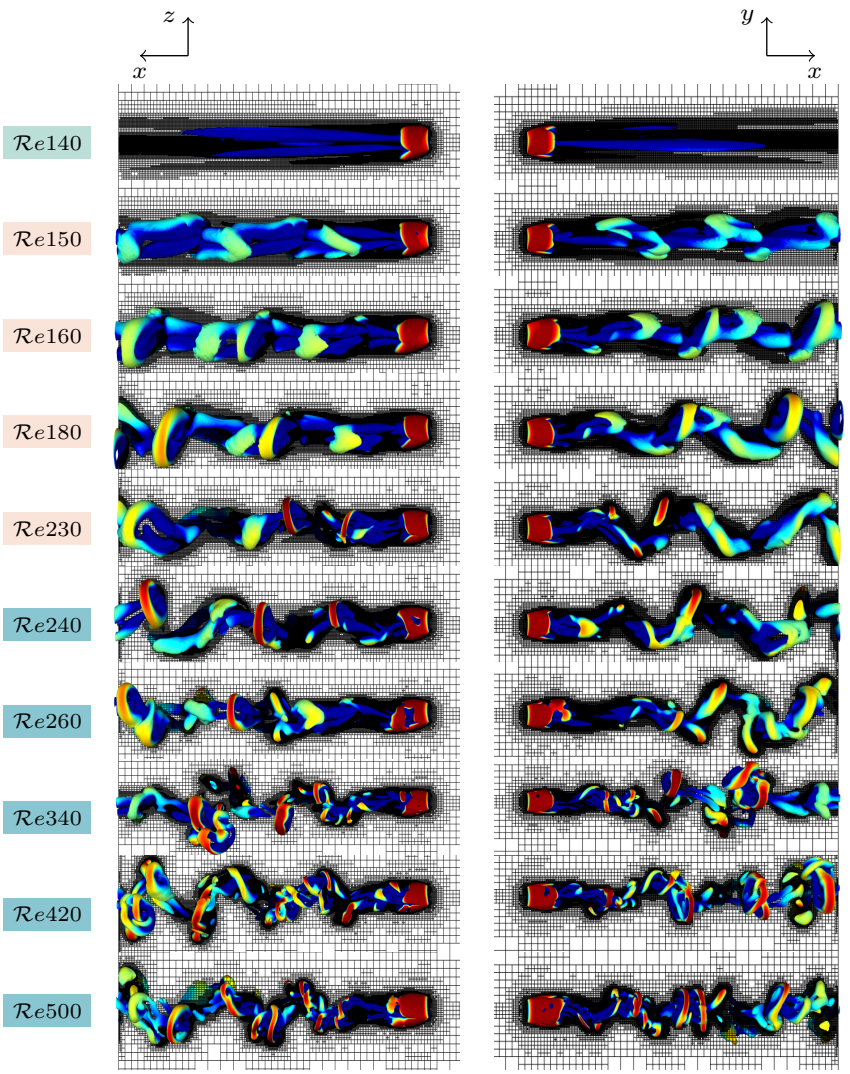

FIG. 15. Wake structures of the flow past a TF, colored by u_x (low velocity in blue and high velocity in red), as a function of Re, identified by the isosurface $\lambda_2 = -1$; views in the x-z plane (left) and the x-y plane (right).

is narrower in the transverse direction than behind the TF tetrahedron, thus leading to smaller and/or slimmer vortex structures. From Re = 260 to Re = 270, we cannot notice clearly the onset of the CS regime from the λ_2 isosurface in the TV case. Quantitative measurements of the transverse force and shedding frequency in the DHS and HS regimes discussed in the following discussion may help to more precisely determine when the transition occurs. In the CS regime, the hairpin structures progressively degenerate as Re increases, and additional small coherent structures appear. In the TF case, the small coherent structures entangle with each other more and more as Re increases until that the large hairpin vortex disappears at Re = 420 in Fig. 15. However, the hairpin vortex structure (with a dominant frequency) remains observable until Re = 500 in Fig. 16 in the TV case, and the additional small coherent vortex structures generated during the vortex shedding are less easily identified in the TV case than in the TF case. We postulate that this is a footprint of the stabilization effects of the front edges of the TV tetrahedron that enhance the flow steadiness.

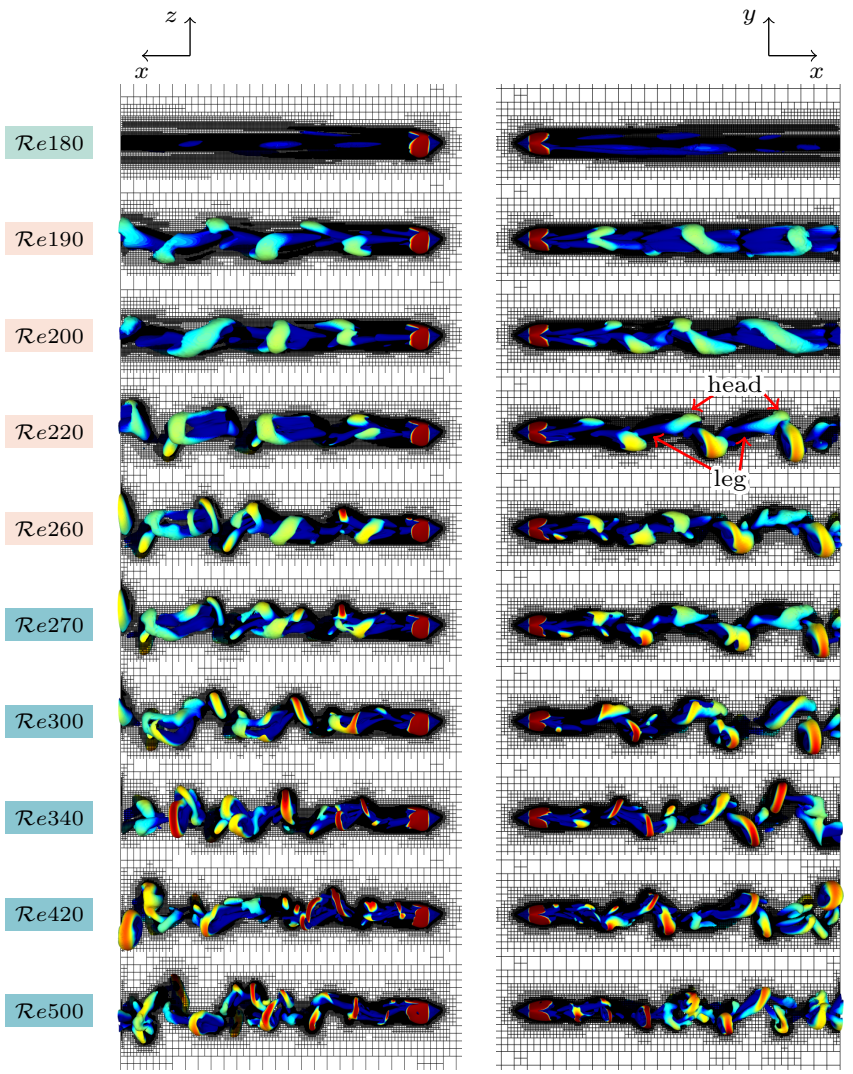

FIG. 16. Wake structures of the flow past a TV, colored by u_x (low velocity in blue and high velocity in red), as a function of Re, identified by the isosurface $\lambda_2 = -1$; views in the x-z plane (left) and the x-y plane (right).

Comparing Figs. 14–16, the λ_2 criterion clearly identifies the vortex flow structures, in particular in the unsteady regimes, and helps to elucidate the strong dependence of the tetrahedron wake region on the tetrahedron angular position. The symmetric DHS is typically original and closely related to the unique angular position of the TE tetrahedron. Let us conclude this section by pointing out that we strongly believe that the observed symmetric DHS regime in the wake of the TE tetrahedron is not a numerical artifact. In particular, the somewhat unexpected sustained symmetry at such large Re of the vortex shedding mechanism is a natural feature of the flow. In fact, looking more closely at Fig. 14, we notice that the octree grid is never perfectly symmetric with respect to the x-y plane and the x-z plane, and therefore this lack of symmetry creates enough numerical disturbance for any instability to grow and to break the flow symmetry if the flow was not symmetric. The fact that the flow remains symmetric even when computed on a nonsymmetric grid constitutes a strong evidence that the flow is physically symmetric in this Re range. To further illustrate the vortex

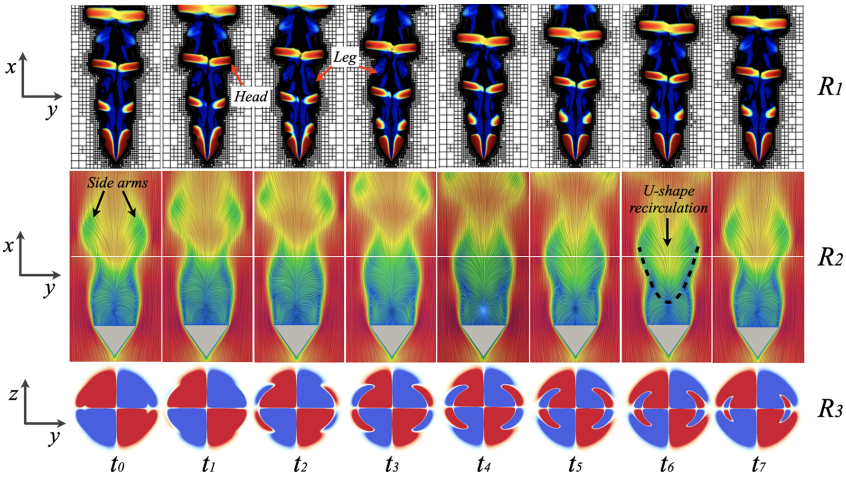

FIG. 17. Symmetric double-hairpin vortex shedding process within a period in the flow at Re = 200 past a TE; (R_1) isosurface of $\lambda_2 = -1$ in the x-y plane at $z = z_p$ colored by u_x; (R_2) LIC of the velocity field in the x-y plane at $z = z_p$, from blue to red denoting the low to high flow velocity; (R_3): streamwise vorticity (positive in red, negative in blue, and $\omega_x \approx 0$ in white) in the particle wake region in the y-z plane at $x = x_p + 1.5$, indicated in a white horizontal line in the row R_2.

structures and provide a more comprehensive understanding of the wake dynamics, we include the side views of the vortices in Appendix C. The visualization in Fig. 28 offers a fully three-dimensional representation of the vortex structures and their spatial distribution, complementing the information presented in the main text.

D. Double-hairpin vortex shedding

Figure 17 depicts the dynamic double-hairpin vortex shedding process in the wake region of the TE tetrahedron at Re = 200 [58]. The first row presents the double-hairpin vortex structures identified by the isosurface $\lambda_2 = -1$ within a single shedding period in the $x - y$ plane. The double-hairpin structure identified by the isosurface $\lambda_2 = -1$ is not *perfectly* symmetric with respect to x axis at Re = 200, but this slight imperfection of the vortex structure symmetry does not lead to any significant lift force exerted on the TE tetrahedron. The flow has a *quasi*orthogonal symmetry and the time average lift coefficient C_l remains close to zero at Re = 200.

Line integral convolution (LIC) is a technique for visualizing the fluid velocity field. Instead of adapting the start and end of streamlines to a specific velocity field, the LIC conveys all structural features of the flow, such as velocity gradient, vortices, and the location of critical points. Row R_2 presents the LIC of the flow field colored by the velocity magnitude in the x-y plane. We note that the *U-shape* recirculation region behind the TE tetrahedron features two long side arms. A pair of hairpin vortex structures is generated simultaneously from the two back corners of the TE tetrahedron (R_3, t_2). They are transported downstream within the recirculation arms and swell by sucking fluid from the outer flow. The volume of the vortices increases at a similar rate such that they keep symmetric to the streamwise central line, i.e., the x axis. However, the vortex pair can hardly grow very large since it can easily detach from the thin arms of the *U-shape* recirculation region. The time for the two vortices to absorb fluid from the surrounding bulk flow is limited, hence the high shedding frequency. On the snapshot (R_2, t_6), when a new vortex pair emerges in the middle section, the previous vortex pair is still attached to the particle wake through the two arms of the *U-shape* recirculation region.

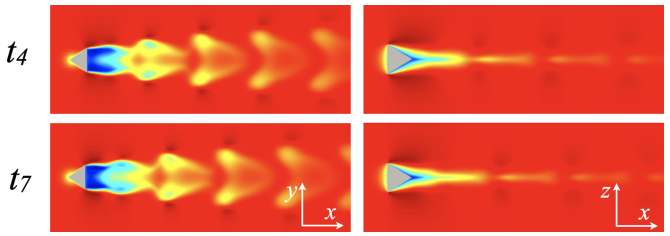

FIG. 18. Countours of u_x in the x-y and x-z planes to identify the recirculation region (blue) in the flow past the TE tetrahedron at Re = 200.

We plot over the row R_3 the streamwise vorticity $\omega_x = \pm 0.03$ in the y-z plane at $x = x_p + 1.5$ in the particle wake at the different discrete times t_i, $i = 0, \ldots, 7$. When a pair of vortices moves downstream of the TE tetrahedron, the vortices display two symmetric crescent vortex structures that attest of the flow symmetry with respect to the y axis during the double-hairpin vortex shedding in a clearer fashion than the λ_2 criterion. The two vortices emerge from the two ends of the vorticity plot along the y axis. The size of the vortex pair first increases while staying on the two ends of the plot (t_0–t_3). From row R_2, we see that this corresponds to the transport of the vortex pair within the two side arms of the recirculation region. Then the size of the crescents shrinks while moving to the center (t_4–t_7), as the vortex pair moves farther downstream and detaches from the particle close wake. Once again, the TE tetrahedron is the only angular position in which we observe highly symmetric vortex structures in unsteady flows.

We present in Fig. 18 the recirculation region (blue) of the flow at Re = 200 past the TE tetrahedron, colored by the streamwise flow velocity u_x, identified in the x-y plane at $z = z_p$ and in the x-z plane at $y = y_p$. We select the two times t_4 and t_7 from Fig. 17. The view in the x-y plane in Fig. 18 illustrates very visibly the *U-shape* recirculation region and the double-hairpin vortex within the two side arms. In contrast, the recirculation region is exceedingly slim and short in the x-z plane in Fig. 18. The two rear faces guide the flow to converge smoothly and narrow down the region for possible backflows. The short blue tail in the x-z plane corresponds to the middle section of the recirculation in the x-y plane. The flow rectification by the two rear faces pushes the fluid to the middle section, increases the local fluid velocity and reshapes the recirculation region. Close to the two rear tips, the flow-rear surface interaction time is shorter and thus the rectification effect correspondingly fades. Consequently, the two side arms are longer than the middle section in the x-y plane leading to the *U-shape* recirculation and the unique double-hairpin vortex shedding.

Another consequence of the *U-shape* recirculation is the reverse double hairpin structure with respect to the streamwise direction. During the formation of the double-hairpin vortex, the hairpin head is generated in the two side arms while the hairpin legs are formed in the middle section of the *U-shape* recirculation region. From Figs. 17 and 18, we know that the velocity in the two side arms is lower than that in the middle section. Compared to the hairpin heads, the hairpin legs are transported at a higher velocity within the *U-shape* recirculation leading to the reverse hairpin structure in the DHS regime. Once leaving the *U-shape* recirculation region, the double-hairpin structure is transported downstream at a similar velocity. Thus, in Fig. 14, the hairpin heads are always located behind the hairpin legs in the TE tetrahedron wake flow.

E. Hydrodynamic forces

In this subsection we examine the time average and time evolution of the drag force along the streamwise direction and the lift force in the transverse plane exerted on the tetrahedron as a function of its angular position.

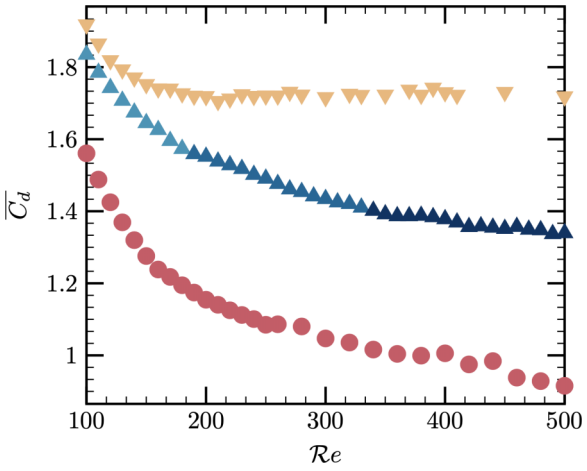

FIG. 19. Time-averaged $\overline{C_d}$ as a function of Re of the flow past a tetrahedron at the three angular positions: TE (▲, ▲, ▲), TF (▼), and TV (●).

1. Drag and lift coefficients

We plot in Fig. 19 the time-averaged drag coefficient $\overline{C_d}$ as a function of Re for the three angular positions. In general, $\overline{C_d}$ decreases with increasing Re but the angular position has a strong impact on the magnitude of $\overline{C_d}$ and the functional form of the dependence on Re. The regime transitions can also be perceived in the drag coefficient evolution, although in a manner less clear than in the vortex structure visualization. Figure 19 shows that $\overline{C_{d,F}} > \overline{C_{d,E}} > \overline{C_{d,V}}$ for any Re $\in [100, 500]$. Note that the tetrahedron has the same streamwise cross-sectional surface area in the TF case and in the TV case. The difference in $\overline{C_d}$ therefore mainly comes from the particle angular position, i.e., the difference of the front and rear surface angularity between the TF case and the TV case. It is also noticeable in Fig. 19 that the effect of particle angular position on $\overline{C_d}$ is more marked at high Re. For instance, the ratio of the drag coefficients $\overline{C_{d,F}}/\overline{C_{d,V}}$ increases from 1.22 at Re $= 100$ to 1.91 at Re $= 500$. As expected, the three front edges and three front surfaces of the TV tetrahedron reduce significantly the exerted drag force, especially in the CS regime.

Regime transitions can be somewhat discerned from the slope variation of the $\overline{C_d}$(Re) plots in Fig. 19. In the TE case, we notice three different Re subintervals. From Re $= 100$ to Re $= 180$ corresponding to the OSS regime and plotted with ▲, $\overline{C_d}$ decreases with a high slope. Then the DHS regime starts at Re $= 190$ and lasts until Re $= 360$, and the slope of the $\overline{C_d}$(Re) curve plotted with ▲ slightly reduces. The CS regime starts when Re $\geqslant 370$ and the slope of the $\overline{C_d}$(Re) plotted with ▲ reduces even more. We observe a similar tendency in the TV case. The slope of the $\overline{C_d}$(Re) curve is the same in the PSS regime and the HS regime, spanning the range Re $= 160$ to Re $= 260$, and is smaller than that in the TSS regime $100 \leqslant$ Re $\leqslant 150$ and larger than that in the CS regime Re $\geqslant 270$. In the TF case, the transitions from the TSS regime to the PSS regime, from the PSS regime to the HS regime and eventually from the HS regime to the CS regime all occur at a smaller Re than in the TV case. However, the TF tetrahedron exhibits a unique feature on the $\overline{C_d}$(Re) curve in the CS regime. In fact, when the HS regime breaks down, $\overline{C_{d,F}}$ stops decreasing with Re from Re $= 240$ and remains approximately constant throughout the CS regime. The TF tetrahedron is the angular position that leads to the largest $\overline{C_d}$ and is also the stable angular position of a freely falling tetrahedron [30,37]. In particular, the trend of our computed $\overline{C_d}$(Re) in the TE case is perfectly in line with the experimental data reported in [37]. The widely used correlation proposed in [37] predicts a value of $\overline{C_d} \approx 2$ when $100 \leqslant$ Re $\leqslant 500$ in the case of the freely settling tetrahedron. This value is slightly larger than our computed value of ≈1.7 in the TF case. This difference is fully understandable. In fact, the face down being the stable position of the freely falling tetrahedron is

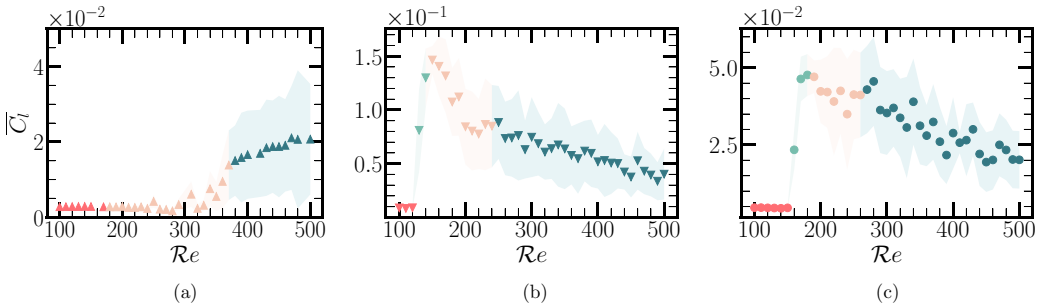

FIG. 20. Time-averaged $\overline{C_l}$ as a function of Re of the flow past a tetrahedron at the three angular positions: TE (▲), TF (▼) and TV (●): multiaxis steady symmetry ( ), planar steady symmetry ( ), periodic vortex shedding ( ), and chaotic vortex shedding ( ); the standard deviation $\sigma(\overline{C_l})$ is represented by the shaded light colored area. (a) TE, (b) TF, and (c) TV.

true on average in time only and the freely falling tetrahedron also experiences transverse motion [30] that slows it down, thus contributing to a slower settling velocity for the same driving force (i.e., net weight) and therefore a higher $\overline{C_d}$ compared to that in the case the tetrahedron is forced to settle with a fixed face down angular position, which would be the reverse problem of the flow past a fixed TE tetrahedron studied here.

We plot in Fig. 20 the time-averaged lift coefficient $\overline{C_l}$ as a function of Re at the three angular positions TE/TF/TV in different flow regimes. In the TE case, $\overline{C_l}$ remains close to zero in the OSS and DHS-I regimes for Re $\leqslant 300$, before increasing in the DHS-II and CS regimes. In the TF and TV cases, the evolution of $\overline{C_l}$ exhibits clear regime transitions. In the TSS regime, $\overline{C_l}$ is close to zero, then increases in the PSS regime and reaches a maximum value during the transition from the PSS regime to the HS regime, as shown in Figs. 20(b) and 20(c). It is noteworthy that the maximum value of $\overline{C_l}$ in the TF case is almost three times higher than that in the TV case, and that $\overline{C_l}$ in the TF case is generally higher than that in the TE and TV cases for a given Re. In general, the symmetry breakup of the wake flow is characterized by an increase in $\overline{C_l}$. Specifically, in the DHS regime, $\overline{C_l}$ increases with increasing Re, while in the HS regime, $\overline{C_l}$ decreases with increasing Re. At a higher Re, the time evolution of C_l exhibits a large standard deviation in all three cases in the CS regime, as shown in Fig. 20. Note that the standard deviation $\sigma(\overline{C_l})$ is represented by the shaded light colored area. For further insight, we refer the reader to our previous study [53] where we investigated the evolution of the time-averaged lift coefficient $\overline{C_l}$ of Platonic polyhedrons at low Re $\leqslant 200$.

Figures 21(a) and 21(b) present the time evolution of C_d and $C_{l,z}$ in the TE case at Re $= 330$ and Re $= 340$. After the breakup of the planar symmetry in the DHS-I regime, $C_{l,z}$ increases noticeably at Re $= 340$ in Fig. 21(b) and indicates the onset of the DHS-II regime. Meanwhile, $C_{l,y}$ remains small due to the symmetric DHS in the x-y plane. It is hard if not impossible to discern this regime transition in the time evolution of C_d in Fig. 21(a). We plot in Figs. 21(c) and 21(d) the maximal/minimal $C_{l,y}$ and $C_{l,z}$ as a function of Re. At Re $= 290$, the magnitude of $C_{l,y}$ starts to increase, indicating the transition from the *quasi*orthogonal symmetric shedding mode to the planar symmetric shedding mode. This mode change in the DHS-I regime does not affect $C_{l,z}$. Please note the factor of 10^{-2} at the top of the vertical axis in Fig. 21(c) such that the values of $C_{l,y}$, while nonzero, remain very small when Re $\geqslant 290$. Then, the breakup of the planar symmetry (onset of DHS-II regime) at Re $= 340$ is well captured by the rise of $C_{l,z}$ at Re $= 340$ in Fig. 21(d). The z axis is the axis perpendicular to the hairpin vortex shedding plane, therefore $C_{l,z}$ is significantly larger than $C_{l,y}$. The maximal/minimal values of $C_{l,z}$ increase in magnitude with Re in the DHS-II regime and then remain approximately constant in the CS regime for Re $\geqslant 370$.

Figure 22 presents the time evolution of $C_{l,y}$ in the TF case at various Re. Since the vortex shedding plane is not aligned with either the x-y plane or the x-z plane, the time evolution of $C_{l,y}$

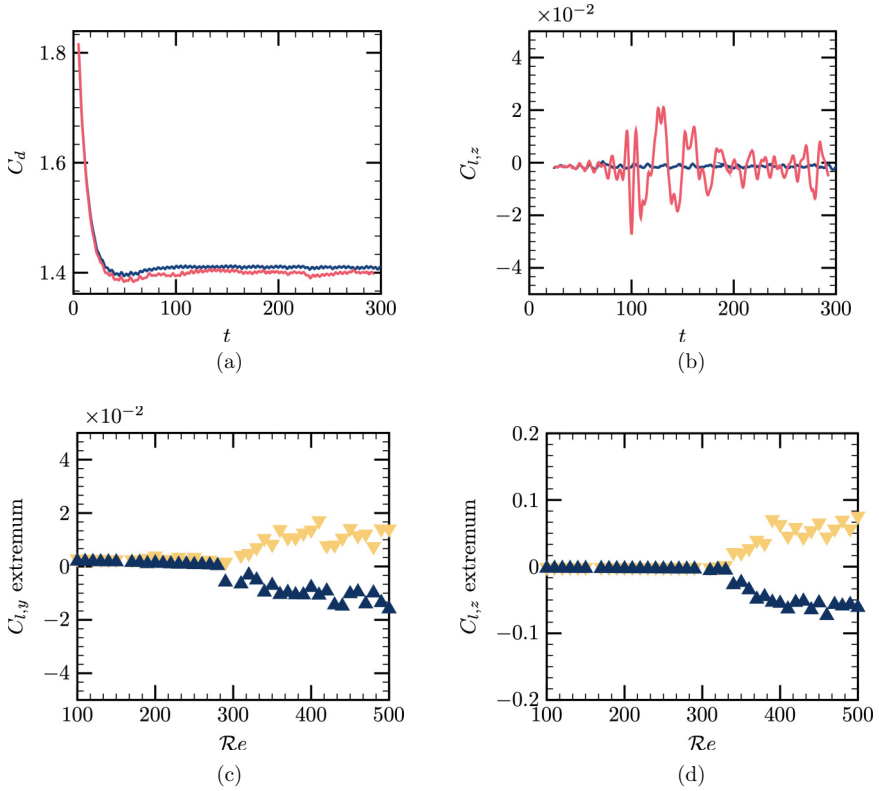

FIG. 21. Flow past the TE tetrahedron: (a), (b) time evolution of C_d and $C_{l,z}$ at Re = 330 (—) and Re = 340 (—), and (c), (d) maximal lift coefficient (▼) and minimal lift coefficient (▲) ($C_{l,y}$ and $C_{l,z}$) as a function of Re.

and the time evolution of $C_{l,z}$ resemble each other and we choose to discuss $C_{l,y}$ as representative. In general, the time required to establish the flow regime decreases with Re, e.g., the CS regime is established faster than the PSS regime. However, the HS regime requires a particularly long time to

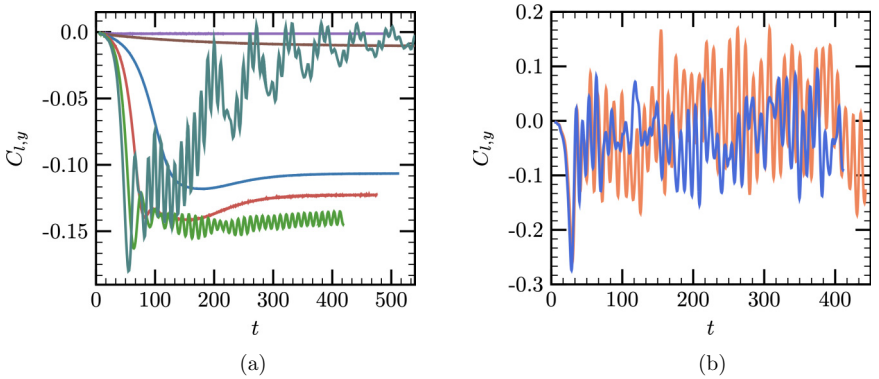

FIG. 22. Time evolution of $C_{l,y}$ in the flow past the TF tetrahedron at Re = 110 (—), Re = 120 (—), Re = 130 (—), Re = 140 (—), Re = 150 (—), Re = 160 (—), Re = 230 (—), and Re = 240 (—).

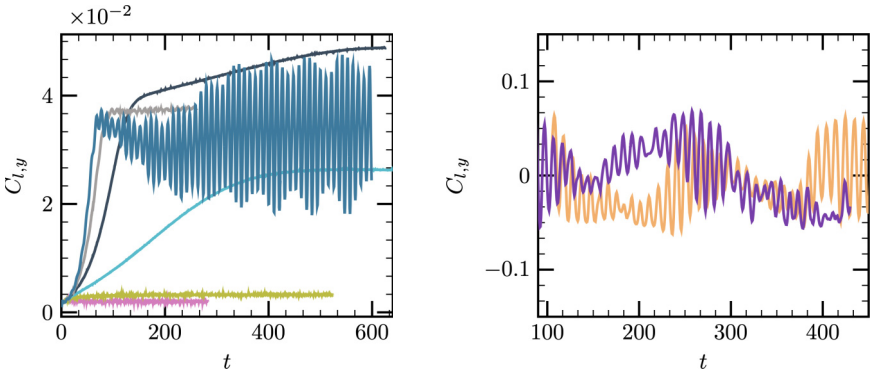

FIG. 23. Time evolution of $C_{l,y}$ in the flow past the TV tetrahedron at Re = 140 (——), Re = 150 (——), Re = 160 (——), Re = 170 (——), Re = 180 (——), Re = 190 (——), Re = 260 (——), and Re = 270 (——).

establish when Re is slightly above the transition to the HS regime. As an illustration, Fig. 22 shows that the flow at Re = 140 needs about $t = 300$ to establish while it needs $t = 400$ at Re = 160 to establish the HS regime. In the steady regime, $C_{l,y}$ increases and reaches a nonzero stable value at Re = 130 and Re = 140. The onset of the HS regime occurs between Re = 140 and Re = 150 in Fig. 22(a). At Re = 160, $C_{l,y}$ decreases to -0.18 in the early transient flow, then oscillates while its time average value converges back to zero. When Re > 160, $C_{l,y}$ oscillates around a time average value close to zero. Figure 22(b) presents the time evolution of $C_{l,y}$ at Re = 230 and Re = 240 corresponding to the transition from the HS regime to the CS regime. Even though the oscillation amplitude of $C_{l,y}$ is pretty similar at Re = 230 and Re = 240, $C_{l,y}$ has a single dominant oscillation frequency at Re = 230 while a secondary oscillation frequency emerges at Re = 240 at the start of the CS regime.

Finally, Fig. 23 presents the time evolution of $C_{l,y}$ in the TV case at various Re. The TF and TV angular positions break the orthogonal symmetry of the flow and thus produce a nonzero lift coefficient even in the low Re steady-state regime. Indeed, $C_{l,y}$ is small but not zero at Re = 140 and Re = 150. At the start of the PSS regime, $C_{l,y}$ increases to a stable value $\approx 2.6 \times 10^{-2}$, $\approx 4.9 \times 10^{-2}$, and $\approx 3.7 \times 10^{-2}$ at Re = 160, Re = 170, and Re = 180, respectively. The onset of the HS regime at Re = 190 translates into rather large amplitude oscillation of $C_{l,y}$ around a nonzero time average value of $\approx 3.7 \times 10^{-2}$. The transition from the periodic HS regime to the CS regime occurs between Re = 260 and Re = 270. Similarly to the TF case, $C_{l,y}$ exhibits a single dominant oscillation frequency in the HS regime at Re = 260 while a secondary oscillation frequency manifests at Re = 270 in Fig. 23(b), indicating the onset of the CS regime. We acknowledge that the emergence of the secondary oscillation frequency is not always overly obvious in the time evolution of the lift coefficients. The role played by the vortex shedding frequency in the determination of the regime transitions is discussed in details in Sec. IV F. Overall, the lift coefficient magnitude never exceeds 10% of the drag coefficient C_d in the Re range and the three tetrahedron angular positions investigated in this study.

2. Vortex shedding patterns

To further investigate the lift force time evolution, we plot $C_{l,y}$-$C_{l,z}$ phase diagrams in Fig. 24. These phase diagrams provide additional comprehension of the time evolution of the transverse forces and the associated vortex shedding pattern in the wake of the tetrahedron at the three angular positions. From purple to red, the rainbow color of the plots indicates time increase. In the steady regime, both $C_{l,y}$ and $C_{l,z}$ are very small due to the multiaxis symmetry of the flow in the OSS and TSS regimes. At a higher Re, the flow becomes unsteady and more complex patterns are

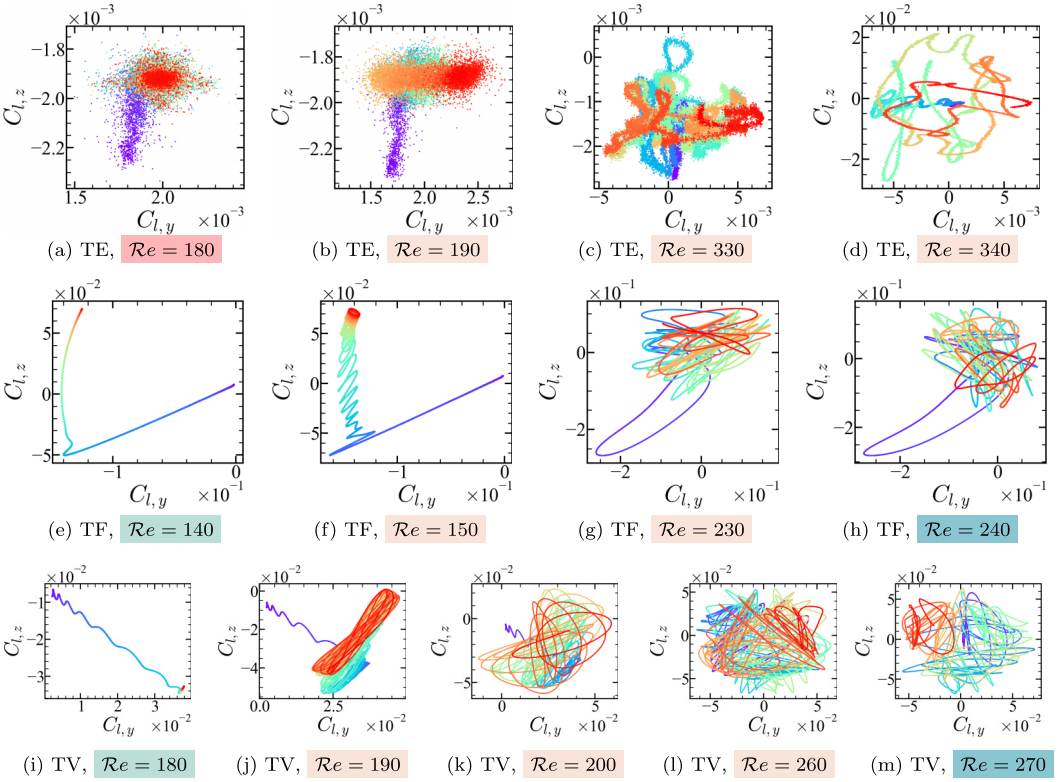

FIG. 24. $C_{l,y}$-$C_{l,z}$ phase diagrams at the three angular positions. Time evolution shown in rainbow colors from purple (start time) to red (end time).

depicted in Fig. 24. In the TE case, from Figs. 24(a) and 24(b), the onset of the DHS-I regime does not significantly change the magnitude of $C_{l,y}$ and $C_{l,z}$. This holds for $190 \leqslant \mathrm{Re} \leqslant 280$ since the wake flow features a *quasi*orthogonal symmetry. From $\mathrm{Re} = 290$ to $\mathrm{Re} = 330$, the second stage of the DHS-I regime features a planar symmetry only in the wake flow and $C_{l,y}$ slightly increases. Figures 24(c) and 24(d) plots the lift coefficients evolution before and after the breakup of the planar symmetry, i.e., the beginning of the DHS-II regime. At $\mathrm{Re} = 340$, the magnitude of $C_{l,z}$ becomes markedly larger than that of $C_{l,y}$. While both $C_{l,y}$ and $C_{l,z}$ oscillate around zero in Fig. 24(d), the oscillation amplitude of $C_{l,z}$ is larger than that of $C_{l,y}$.

The lift coefficients behave differently in the TF and TV cases. In the PSS regime, $C_{l,y}$ and $C_{l,z}$ reach stable values after a long enough simulation time as shown in Figs. 24(e) and 24(i). In the steady state, the lift curve stays in the red dot region and no longer moves. With the onset of HS, the lift coefficients start to oscillate around nonzero time average values. For instance, the path is oval in Fig. 24(f) for the TF tetrahedron and shaped as a tilted ∞ in Fig. 24(j) for the TV tetrahedron. Different from the flow past a sphere or a cube, the shedding plane is not stationary and rotates around the x axis in time and with the increase of Re for both the TF tetrahedron and the TV tetrahedron. In the TF case at $\mathrm{Re} = 230$ in Fig. 24(g), the oscillation amplitude of $C_{l,y}$ is larger than that of $C_{l,z}$. In the TV at $\mathrm{Re} = 200$ in Fig. 24(k), the shedding plane oscillates around the x axis with a maximal rotation angle of about $\pi/2$ and an oscillation period of about $t = 100$. Considering the triangular shape of the cross-sectional surface area in the TF vase and the TV case, the wake flow from the three cross-sectional edges converges at the rear vertex or the rear face, respectively. The streams coming from three directions are hard to stabilize at high Re and conversely promote a rotating vortex shedding. In the late stage of the HS regime, the rotation of

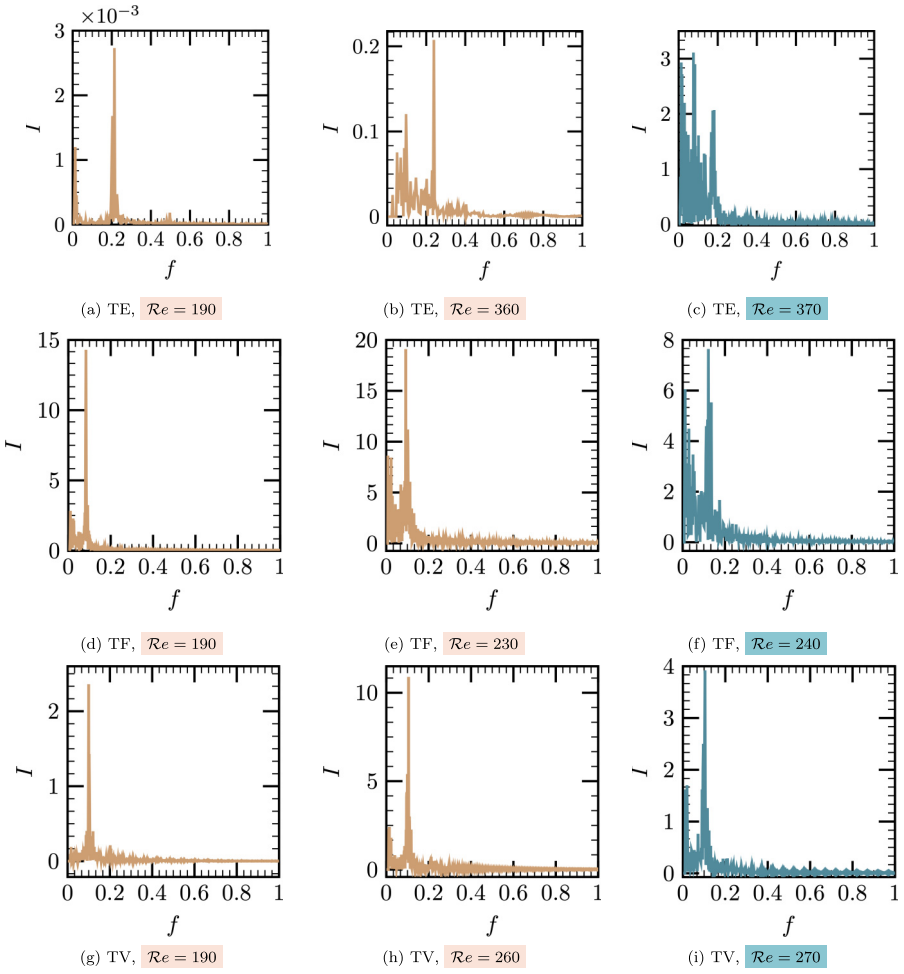

FIG. 25. Dimensionless vortex shedding frequency f spectrum in the periodic HS/DHS regime and the CS regime. I denotes the dimensionless intensity of the frequency obtained through FFT.

the vortex shedding plane becomes less organized and the vortex shedding plane angular position changes intermittently in time. This lack of organization increases even more as soon the CS regime starts at Re = 270 as shown in Fig. 24(m). Once the CS regime starts, the flow structures in the particle wake region become more cluttered. At Re = 240 in the TF case, the lift coefficients no longer have any privileged direction in the phase diagram in Fig. 24(h). Similarly, in the TV case, we note in Fig. 24(m) that the time evolution of $C_{l,y}$ and $C_{l,z}$ becomes highly disorganized. The phase diagram in Fig. 24(m) resembles that in Fig. 24(l). In the CS regime, $C_{l,y}$ and $C_{l,z}$ have a similar oscillation amplitude.

F. Vortex shedding frequency

We now examine the frequency of the hairpin vortex detachment from the particle rear surface. In the flow past a sphere or a cube, the dominant frequency of the vortex shedding is reported to be around St = 0.1 [17,35].

We plot in Fig. 25 the frequency spectrum ($f = f^* D^*_{\text{sph}}/U^*_0$) of the time evolution of C_d in the TE case and of $C_{l,y}$ (or $C_{l,z}$) in the TF and TV cases. These frequency spectra are computed by classical fast Fourier transform (FFT). To obtain an accurate and representative estimation of the

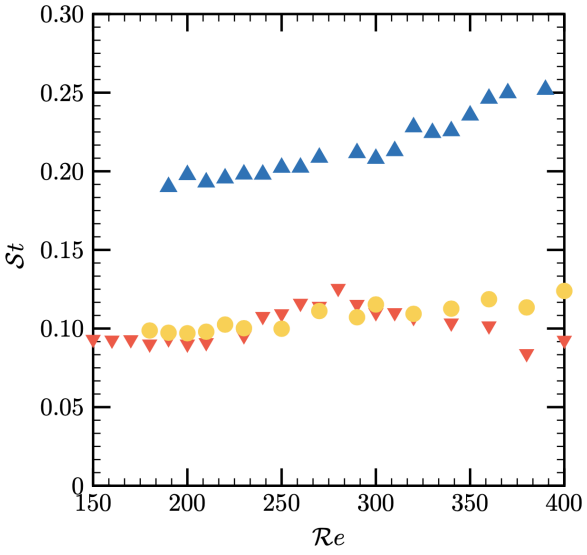

FIG. 26. St as a function of Re at the three angular positions: TE (▲), TF (▼), and TV (●).

dominant frequency, we choose a number of periods in the time evolution of the flow once vortex shedding regime is well established. Please note that in the CS regime, the dominant frequency slightly varies with the time interval chosen in the FFT computations since the shedding is highly disorganized. Consequently, we report approximate values only of the dominant frequency (and St) in the CS regime. Comparing Figs. 25(a), 25(d), and 25(g), we note that the dominant frequency of the DHS regime past a TE tetrahedron is twice ($f \approx 0.2$) that in the HS regime past a TF tetrahedron and a TV tetrahedron ($f \approx 0.1$). At the end of the DHS-II regime at Re $= 360$ in the TE case, Fig. 25(b) exhibits several low-frequency peaks while the dominant frequency is still about $f \approx 0.23$. Similarly, at the end of the HS regime (Re $= 230$ in the TF case and Re $= 260$ in the TV case), the dominant frequency remains $f \approx 0.1$. Generally, the dominant frequency remains almost constant throughout the periodic DHS and HS regimes. In the CS regime, the dominant shedding frequency seems to become lower than 0.2 at Re $= 370$ in the TE case in Fig. 25(c). In the TF and TV cases, the dominant frequency remains close to 0.1, but its intensity decreases and various secondary peaks arise as depicted in Figs. 25(f) and 25(i). The appearance of a secondary low-frequency peak is observed in the late stage of the periodic vortex shedding regime, specifically in the DHS regime for the TE case and the HS regime for the TF and TV cases. As seen from Figs. 25(b), 25(e), and 25(h), in the periodic shedding regime, the intensity of the secondary peak is lower compared to the dominant peak. This secondary peak is associated with the low-frequency dynamics of the wake vortices, which is also reflected in the temporal evolution of the lift coefficient $\overline{C_l}$, as shown in Fig. 22(a). The evolution of the low-frequency peak with Re indicates a gradual transition from the periodic shedding regime to weak turbulence. This observation is consistent with the findings of Meng *et al.* [35], who also reported the presence of physically relevant low-frequency peaks in the flow past a fixed cube and divided the HS regime into two subregimes accordingly.

Figure 26 shows the evolution of the Strouhal number St as a function of Re for the three angular positions for $150 \leqslant \text{Re} \leqslant 400$, i.e., we mainly focus on the hairpin vortex shedding regime and the early stage of the CS regime. In the early stage of the CS regime, we count the number of hairpin vortices detached from the particle over a given time interval to obtain an approximative value of St, considering that the shedding frequency of the main hairpin structure may not be dominant in the CS regime. Please note that such a computation in the CS regime leads to slightly different value of

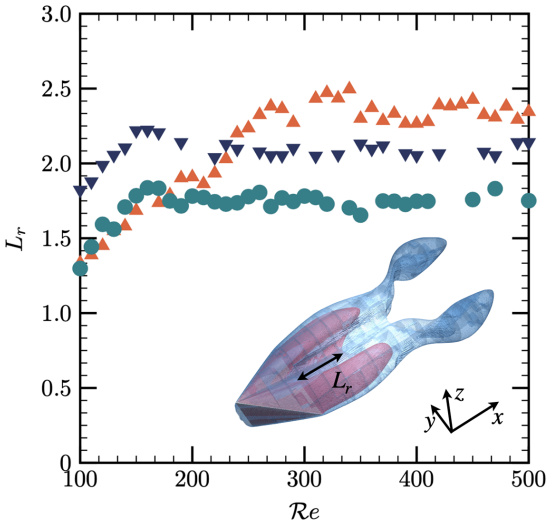

FIG. 27. Recirculation region length L_r as a function of Re of flow past a tetrahedron at the three angular positions: TE (▲), TF (▼), TV (●). Inset: 3D *U-shape* recirculation region (red) and $u_x = 0.5$ isosurface (blue) in the wake of the TE at Re = 200.

St than that given by simply identifying the highest intensity frequency mode in the FFT computed frequency spectra presented in Fig. 25.

In the TF and TV cases, the HS regime starts at Re = 150 and Re = 190, respectively and St remains approximately constant around 0.1 up to Re = 400. This value was also reported by [35] in the unsteady flow past a fixed cube. When Re increases, the flow transitions to the CS regime, where multiple high-intensity frequencies arise and vary in time. In the CS regime, St shows a very mild tendency to increase with Re in the TV case, while it first slightly increases with Re for $240 \leqslant \mathrm{Re} \leqslant 280$ and then slightly decreases for $\mathrm{Re} \geqslant 290$ in the TF case. Overall, in the TF and TV cases, the variation of St with Re is not significant and the dominant dimensionless frequency remains close to St = 0.1.

In the TE case, the DHS regime starts at Re = 190 with $\mathrm{St} \approx 0.2$, indicating again that the DHS regime is twice faster than the HS regime. St slowly increases with Re from Re = 190 to Re = 400. In the DHS-I and DHS-II regimes where vortex shedding is easily identified, the highest intensity frequency mode in the FFT computed frequency spectra method and the vortex shedding counting method deliver similar values of St. Indeed, the increase of St with Re is also noticeable when we compare Fig. 25(a) and Fig. 25(b). However, in the CS regime, the value of St delivered by the vortex shedding counting method does not correspond to the highest intensity frequency mode in Fig. 25(c). This observation attests again of the difficulty of properly estimating the vortex shedding frequency in the CS regime. Nevertheless, as discussed in Sec. IV D, the high shedding frequency of the TE tetrahedron is due to the *U-shape* recirculation region. The two side arms of the *U-shape* recirculation region have a limited volume that restricts the time available to the double-hairpin vortices to grow and promotes vortex detachment. At $\mathrm{Re} \geqslant 400$, the hairpin vortex structures are too disorganized to be properly identified and the computation of St may not be valid anymore.

G. Length of the recirculation region

We plot in Fig. 27 the time average dimensionless length of the recirculation region $L_r = L_r^*/D_{\mathrm{sph}}^*$ as a function Re for the three angular positions. Different from the convex oval shape in a streamwise cut plane of the recirculation region behind a sphere or a cube, the TE tetrahedron exhibits a *U-shape* recirculation region, where the two sides are longer than the middle section. For consistency, L_r denotes the length of the longest section in the recirculation region. In Fig. 27, we note that L_r

TABLE IV. Symmetry and dynamic features of flow with different Re past a tetrahedron at three angular positions (TE, TF, TV): multiaxis steady symmetry ( ), planar steady symmetry ( ), periodic vortex shedding ( ), and chaotic vortex shedding ( ).

A.P.	$\mathcal{R}e$	State	Symmetry	Dynamic features
Edge	$100 \leq \mathcal{R}e \leq 180$	OSS	Orthogonal symmetry	Steady, lift-free four counter-rotating wake vortices
	$190 \leq \mathcal{R}e \leq 280$	DHS-I	*Quasi*-orthogonal symmetry	Double-hairpin vortex lift-free, single-frequency shedding
	$290 \leq \mathcal{R}e \leq 330$	DHS-I	Planar symmetry	Double-hairpin vortex secondary-frequency
	$340 \leq \mathcal{R}e \leq 360$	DHS-II	Asymmetry	Double-hairpin vortex multiple frequencies
	$370 \leq \mathcal{R}e \leq 500$	CS	Asymmetry	Chaotic shedding
Face	$100 \leq \mathcal{R}e \leq 120$	TSS	Tri-planar symmetry	Steady
	$130 \leq \mathcal{R}e \leq 140$	PSS	Planar symmetry	Steady, lift-free two counter-rotating wake vortices
	$150 \leq \mathcal{R}e \leq 230$	HS	Planar symmetry	Hairpin vortex shedding secondary frequency
	$240 \leq \mathcal{R}e \leq 500$	CS	Asymmetry	Chaotic shedding
Vertex	$100 \leq \mathcal{R}e \leq 150$	TSS	Tri-planar symmetry	Steady
	$160 \leq \mathcal{R}e \leq 180$	PSS	Planar symmetry	Steady, lift-free two counter-rotating wake vortices
	$190 \leq \mathcal{R}e \leq 260$	HS	Planar symmetry	Hairpin vortex shedding secondary frequency
	$270 \leq \mathcal{R}e \leq 500$	CS	Asymmetry	Chaotic shedding

first increases with Re for $100 \leqslant \mathrm{Re} \leqslant 330$, i.e., in the OSS and DHS-I regimes, and then remains constant about 2.3 for $\mathrm{Re} \geqslant 340$, i.e., in the DHS-II and CS regimes. With increasing Re, the middle section of the recirculation region shrinks gradually and disappears intermittently. For $\mathrm{Re} \geqslant 250$, the recirculation region splits in two, and the middle section can hardly be seen anymore.

In the TF and TV cases, the evolution of L_r with Re is very similar. L_r increases with Re in the steady regimes and then remains constant in the unsteady HS and CS regimes. We report that $L_r \approx 1.7$ in the TF case and $L_r \approx 2.0$ in the TV case. We also note that while the recirculation region is longer in the streamwise direction in the TV case than in the TF case, the recirculation region is wider in the transverse direction in the TF case than in the TV case. In the HS regime, the detachment of the vortices occurs at the rear side of the oval recirculation region in the TF and TV cases. In contrast, we see from Fig. 17 that the detachment of the double-hairpin vortices in the TE case takes place in the two side arms. As a result, L_r provides a rough estimate of the location of vortex detachment in unsteady flows.

V. SUMMARY AND CONCLUSION

We provided a comprehensive picture of the different regimes of the flow past a fixed regular tetrahedron at three angular positions: face facing the flow (TF), edge facing the flow (TE), and vertex facing the flow (TV), and at Reynolds number $100 \leqslant \mathrm{Re} \leqslant 500$. We analyzed and determined the two well-known regime transitions: loss of symmetry of the wake and loss of stationarity of the flow as a function of Re. The symmetry characteristics and dynamic features of the flow in different regimes are summarized in Table IV. This work is a step towards understanding the effects of particle angularity on the flow regime transitions.

We showed that regime transitions are very sensitive to the tetrahedron angular position. In the steady regime, several pairs of opposite-signed vortices appear in the wake region and the number

of pairs is closely related to the geometry of the particle front surface. The vortices have leglike tails expanding with Re into the wake region and then become perturbed and fluctuate. The multiaxis symmetry breaks into a planar symmetry for all three angular positions. In the particle wake region, the recirculation length L_r increases with Re in steady flows and then remains constant in unsteady flows. The TE tetrahedron features a nonconvex *U-shape* recirculation region that differs from the oval recirculation region of the other two angular positions. We presented a detailed analysis of the vortex structure and the forces exerted on the tetrahedron. We also estimated the critical Reynolds numbers corresponding to the regime transitions. We identified a new shedding mode in the flow past the TE tetrahedron that we called symmetric double-hairpin vortex shedding. Three remarkable features are noticed in the double-hairpin vortex shedding:

(i) the high level of geometric symmetry of the TE tetrahedron (orthogonal symmetry) leads to a high level of symmetry in the flow even when the flow is unsteady (*quasi*orthogonal symmetry or planar symmetry);

(ii) a dominant frequency ($\mathrm{St} \approx 0.2$) twice larger than that in single-hairpin vortex shedding ($\mathrm{St} \approx 0.1$) observed in the flow past a sphere, a cube or a tetrahedron at other two angular positions;

(iii) a reverse structure of the double-hairpin vortices compared to the single-hairpin vortices, i.e., the double-hairpin legs have a leading position with respect to the hairpin heads in the downstream flow.

The formation of the double-hairpin vortex shedding is due to the unique *U-shape* recirculation region in the wake of the TE tetrahedron. The recirculation region shape is a reflection of the particle angularity and angular position in the fluid flow, and determines the vortex structures and their shedding properties. The single-vortex structures in the TF and TV cases are very similar to those found in the flow past a sphere or a cube, except that they are slightly slimmer in the TV case. We also noticed that the plane of the periodic single-hairpin vortex shedding is time-dependent and oscillates around the x axis. In the chaotic regime, the hairpin structures become increasingly disorganized and additional small coherent structures manifest in the wake at all angular positions. The fact that the front surface of the TF tetrahedron is perpendicular to the streamwise direction contributes to the massive generation of small coherent vortex structures and this generation is more evident (or at least occurs at a smaller Re) than in the other two angular positions. The drag coefficient $\overline{C_d}$ of the tetrahedron at all three angular positions decreases with Re. For a given Re, $\overline{C_d}$ of the TF tetrahedron is larger than $\overline{C_d}$ of the TE tetrahedron, that is itself larger than $\overline{C_d}$ of the TV tetrahedron. The lift coefficients $\overline{C_{l,y}}$ and $\overline{C_{l,z}}$ reach their highest values when Re belongs to an interval of values that corresponds to the end of the steady regime and the start of the unsteady regime. In the chaotic vortex shedding regime, the time average lift coefficients are nearly zero at all three angular positions. Usually, the maximal magnitude of the lift coefficient amounts less than 10% of the drag coefficient $\overline{C_d}$.

Among the various methods we used to investigate the regime transitions, the streamwise component of vorticity ω_x and the lift coefficients ($\overline{C_{l,y}}$ or $\overline{C_{l,z}}$) are suitable for the characterization of the steady flows while the λ_2 criterion, the cross-sectional components of vorticity (ω_y or ω_z), and the dominant frequency St provide more insight into the vortex structures of the unsteady flows. We combined multiple methods to determine the critical Reynolds number $\mathrm{Re_{cr}}$ corresponding to the regime transitions, but we were careful in providing estimates of $\mathrm{Re_{cr}}$ with an error bar of ± 5 given the limited data set we generated through highly resolved numerical simulations. Additional simulations at Re around the estimated $\mathrm{Re_{cr}}$, e.g., with a step of 2 in Re instead of a step of 10, might help to estimate the $\mathrm{Re_{cr}}$ with a higher accuracy, although we do not believe that doing so will fundamentally improve our understanding of the flow dynamics.

Our study highlighted the significant effects of the particle shape and particle angular position on the flow dynamics and regime transitions. These regimes, particularly the double-hairpin vortex shedding regime for the TE tetrahedron, are markedly different from those observed in the flow past a sphere. The particle angular position has two observable effects on the regime transition: (i) the sharp edges and inclined faces on the particle front surface generate various patterns of vorticity distribution. The symmetry breakup of the wake flow structures is directly induced by the

interaction of vorticity structures, such as vorticity merging. Consequently, particles with different angular position have different critical Reynolds numbers $\mathrm{Re}_{\mathrm{cr}}$ of symmetry breakup from the OSS/TSS regime to the PSS regime; (ii) the angular position of the particle affects the size and shape of the recirculation region (e.g., *U-shape* in the TE case and oval shape in the TF case) that in turn play a crucial role in the onset of vortex shedding and lead to different $\mathrm{Re}_{\mathrm{cr}}$ values from the PSS regime to the HS/DHS regime and eventually from the HS/DHS regime to the CS regime.

We also acknowledge that the flow past a stationary particle is a simplified flow configuration, yet it reveals highly intricate flow dynamics. In reality, particles are most of the time freely moving in either an otherwise quiescent flow (density difference driven settling) or in an already forced flow (e.g., particle transport in a pipeline or fluidized bed). We already investigated configurations involving angular freely moving particles [27,30,31] but only selected specific shapes. Platonic polyhedrons offer a way to investigate the effect of angularity in a controlled manner, i.e., the sphericity of the angular Platonic polyhedron scales with its number of faces (and a larger number of faces accordingly decreases the sharpness of edges) and the particle remains isometric. We already examined the effect of the number of faces on the drag and lift coefficients in the (mostly) steady flow past a Platonic polyhedron in a previous work [53]. One extension of the present work is to extend [53] to unsteady flows and investigate regimes transitions as a function of the number of faces of a Platonic polyhedron, both in the simple case of the flow past a stationary Platonic polyhedron and in the more exciting case of a freely settling/rising Platonic polyhedron. Another future research avenue involves conducting a proper orthogonal decomposition (POD) or dynamic mode decomposition (DMD) analysis of the vortex shedding behind a tetrahedron at various angular positions to better understand the impact of the sharp edges on the flow. It is also of interest to explore the effect of particle angularity (e.g., via Platonic polyhedrons) on the flow modes. Such additional studies will contribute to figuring out whether a smooth evolution of the flow dynamics exists from a tetrahedron to a sphere through increasing the number of faces of the Platonic polyhedron, with the sphere being the asymptotic case featuring an infinity of faces.

ACKNOWLEDGMENTS

G.G. thanks the Pacific Institute of Mathematical Sciences for their support through his PIMS-CNRS post-doctoral fellowship. The authors greatly appreciate the financial support of the Natural Sciences and Engineering Research Council of Canada (NSERC) via Anthony Wachs New Frontiers in Research Fund Grant No. NFRFE-2018-01922. This research was enabled by support provided by Compute Canada [59] through Anthony Wachs's 2020 and 2021 Computing Resources for Research Groups allocation qpf-764-ac.

APPENDIX A: DISTRIBUTED LAGRANGE MULTIPLIER/FICTITIOUS DOMAIN (DLM/FD) METHOD

The DLM/FD method relies on deriving a combined equation of motion for the fluid-particle mixture obtained by combining the weak formulation of the fluid motion equation and that of the rigid particle. First, the weak formulation for the fluid domain $\Omega \setminus P$ is obtained by enforcing the rigid body constraint (here the tetrahedron is stationary) on the particle surface ∂P. Then the formulation is extended to the computational domain Ω by imposing the rigid body motion constraint in the whole particle P. Associating the weak formulation of the fluid motion equation with that of the rigid particle, we get the *combined weak equation of motion for the entire domain* Ω, for the fluid-particle mixture. Finally, Lagrange multipliers $\boldsymbol{\lambda}^*$ are used to relax the rigid-body motion constraint in the particle P.

We introduce the following functional spaces:

$$\mathcal{W}_\Gamma = \{\boldsymbol{v}^* \in \mathcal{H}^1(\Omega)^3 | \boldsymbol{v}^* = (U_0^*, 0, 0) \text{ on } \Gamma \setminus \text{right}\}, \tag{A1}$$

$$\mathcal{W}_0 = \{\boldsymbol{v}^* \in \mathcal{H}^1(\Omega)^3 | \boldsymbol{v}^* = (0,0,0) \text{ on } \Gamma \setminus \text{right}\}, \tag{A2}$$

$$\mathcal{L}_0^2 = \{q^* \in \mathcal{L}^2(\Omega)^3 | \int_\Omega q^* d\boldsymbol{x} = 0\}, \tag{A3}$$

$$\Lambda = \mathcal{H}^1(P)^3, \tag{A4}$$

and solve in the case of a single stationary particle P the following constrained optimization problem: find $\boldsymbol{u}^* \in \mathcal{W}_\Gamma$, $p^* \in \mathcal{L}_0^2$, and $\boldsymbol{\lambda}^* \in \Lambda$ such that:

(1) Combined equations of motion

$$\int_\Omega \rho_f^* \left(\frac{\partial \boldsymbol{u}^*}{\partial t^*} + (\boldsymbol{u}^* \cdot \nabla)\boldsymbol{u}^* \right) \cdot \boldsymbol{v}^* d\boldsymbol{x} - \int_\Omega p^* \nabla \cdot \boldsymbol{v}^* d\boldsymbol{x} + \int_\Omega \mu_f^* \nabla \boldsymbol{u}^* : \nabla \boldsymbol{v}^* d\boldsymbol{x} = - \int_P \boldsymbol{\lambda}^* \cdot \boldsymbol{v}^* d\boldsymbol{x}, \tag{A5}$$

$$\int_P \boldsymbol{\alpha}^* \cdot \boldsymbol{u}^* d\boldsymbol{x} = 0. \tag{A6}$$

(2) Continuity equation

$$\int_\Omega -q^* \nabla \cdot \boldsymbol{u}^* d\boldsymbol{x} = 0, \tag{A7}$$

for all $\boldsymbol{v}^* \in \mathcal{W}_0$, $q^* \in \mathcal{L}^2(\Omega)$ and $\boldsymbol{\alpha}^* \in \Lambda$. Eventually, we rewrite Eqs. (A5)–(A7) in a nonvariational form that is more amenable to a finite volume (or a finite difference) spatial discretization [50,51].

To solve efficiently the fully coupled Eqs. (A5) and (A6), Selçuk *et al.* [51] used a first-order operator-splitting approach (or fractional step method) to divide the coupled problem into multiple subproblems [60]. This approach was first introduced by Glowinski *et al.* [47] in the context of particle-laden flow computations and later used extensively in many papers, including in our own papers [49–51]. The coupled equations can be regarded as an initial value problem:

$$\frac{d\Phi^*}{dt^*} + \boldsymbol{A}_1(\Phi^*) + \boldsymbol{A}_2(\Phi^*) = f_t^*, \tag{A8}$$

$$\Phi^*(t^* = 0) = \Phi_0^*, \tag{A9}$$

where the operators $\boldsymbol{A}_i$ can be determined differently depending on various splitting strategies [61,62]. Φ^* is a vector of unknown fields $\Phi^* = (\boldsymbol{u}^*, p^*, \boldsymbol{\lambda}^*)$. A two-step splitting strategy is used in the current implementation [50]:

$$\frac{\Phi^{*,n+1/2} - \Phi^{*,n}}{\Delta t^*} + \boldsymbol{A}_1(\Phi^{*,n}, \Phi^{*,n+1/2}) = f_1^{*,n+1}, \tag{A10}$$

$$\frac{\Phi^{*,n+1} - \Phi^{*,n+1/2}}{\Delta t^*} + \boldsymbol{A}_2(\Phi^{*,n+1}) = f_2^{*,n+1}, \tag{A11}$$

$$f_1^{*,n+1} + f_2^{*,n+1} = f_t^*[(n+1)\Delta t^*]. \tag{A12}$$

Symbolically, the operator $\boldsymbol{A}_1$ represents the Navier-Stokes problem where the advection-diffusion equation and the incompressibility condition are solved together. The first subproblem computes $\boldsymbol{u}^{*,n+1/2}$ and $p^{*,n+1/2}$ and takes both $\Phi^{*,n}$ and $\Phi^{*,n+1/2}$ as parameters given that the velocity advection term is treated explicitly while the velocity diffusion term is treated implicitly. The second term $\boldsymbol{A}_2$ denotes the fictitious domain problem with the rigid body motion constraint imposed on the particle, which computes $\boldsymbol{u}^{*,n+1}$ and $\boldsymbol{\lambda}^{*,n+1}$ through the solution of a saddle-point problem for the fluid velocity $\boldsymbol{u}^*$ and the Lagrange multipliers $\boldsymbol{\lambda}^*$. The second problem leaves the pressure p^* unchanged such that $p^{*,n+1} = p^{*,n+1/2}$. This first-order operator-splitting method can provide robust and stable solutions [63]. Additionally, implementing the above approach is convenient as it allows for a wide range of solver options for the subproblems.

TABLE V. Dimensionless vertex coordinates with respect to the mass center of the regular tetrahedron at the three angular positions (A.P.): TE (edge), TF (face), and TV (vertex).

A.P.	Vertex coordinates (x', y', z')
TE	(0.581224, −0.821974, 0.000000)
	(0.581224, 0.821974, 0.000000)
	(−0.581224, 0.000000, −0.821974)
	(−0.581224, 0.000000, 0.821974)
TF	(−0.335570, 0.000000, −0.949134)
	(−0.335570, 0.821974, 0.474567)
	(−0.335570, −0.821974, 0.474567)
	(1.006710, 0.000000, 0.000000)
TV	(0.335570, 0.000000, 0.949134)
	(0.335570, 0.821974, −0.474567)
	(0.335570, −0.821974, −0.474567)
	(−1.006710, 0.000000, 0.000000)
Pyramid	(0.949134, 0.000000, −0.335570)
	(−0.474567, 0.821974, −0.335570)
	(−0.474567, −0.821974, −0.335570)
	(0.000000, 0.000000, 1.006710)

We use the implementation of Ref. [51] in the *open-source* code Basilisk to solve the Navier-Stokes subproblem due to Basilisk's flexible implementation on hierarchically refined Cartesian grids and the remarkable convergence features of its geometric multigrid solver for Poisson/Helmholtz-type problems [54]. The DLM/FD method and the corresponding iterative Uzawa conjugate gradient algorithm [49] are implemented on Basilisk's Cartesian octree grids, which allow a parent cubic cell to be divided into eight subcubes for local grid refinement of specific regions of interest [51]. In a more general problem involving freely moving rigid bodies, an additional granular subproblem is solved using our *in-house* Grains3D solver [64,65], considering its strong capacity to handle collisions between rigid particles of complex shape. The particle motion is turned off in the computations performed in this work since the particle is stationary. Further information on the numerical implementation and validation can be found in the prior works of our group [49–51].

APPENDIX B: VERTEX COORDINATES OF THE REGULAR TETRAHEDRON IN THE THREE ANGULAR POSITIONS

Table V gives the complete list of the dimensionless vertex coordinates, i.e., the vertex coordinates normalized by the equivalent volume sphere diameter, of the regular tetrahedron at the three angular positions. Note that these coordinates (x', y', z') are given with respect to the mass center of the tetrahedron. For the TE tetrahedron, the front edge is parallel to the z axis while the rear edge is parallel to the y axis. Both edges are perpendicular to the streamwise x direction. The TF tetrahedron has a front surface orthogonal to the streamwise x direction. Its rear vertex lies on the x axis and one of the edges on its front surface is parallel to the y axis. In contrast, the TV tetrahedron has mirror symmetry with the TF tetrahedron with respect to the y-z plane at $x' = 0$. It has a front vertex on the x axis and a rear surface perpendicular to the streamwise x direction. Similarly, one of the edges on its rear surface is parallel to the y axis. The 3D view of the three angular positions along the streamwise direction and other geometric features are illustrated in Figs. 5 and 6.

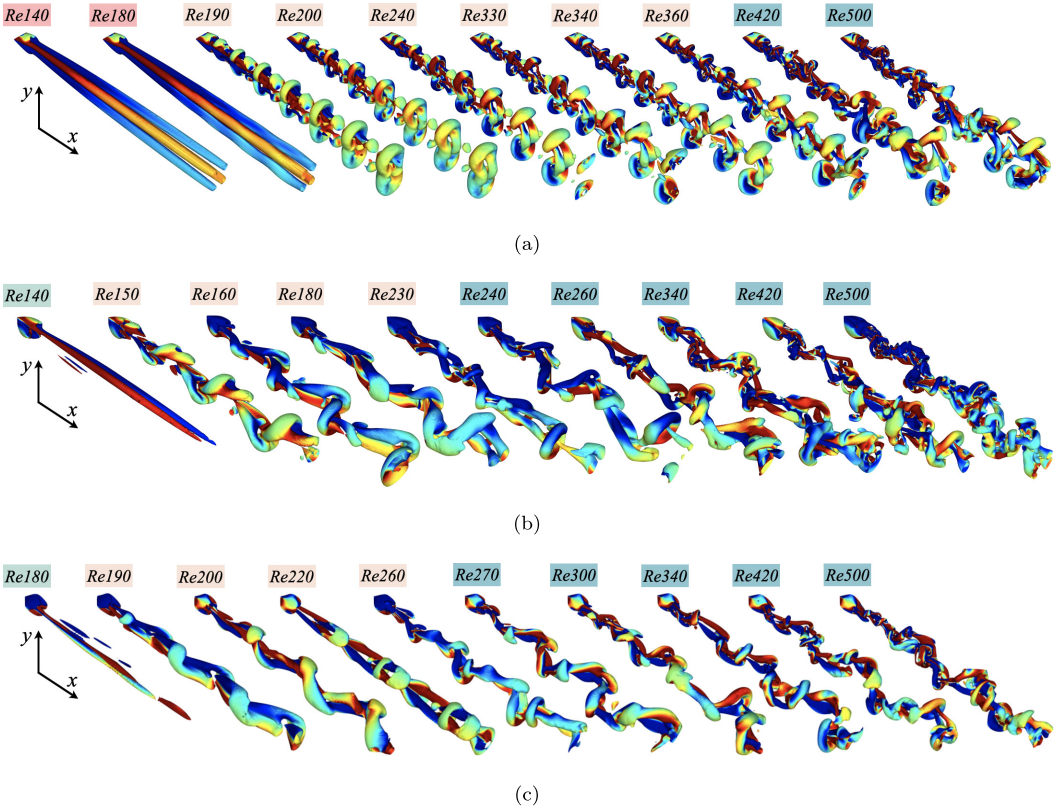

FIG. 28. Side view of wake structures of the flow past a TV, colored by u_x (low velocity in blue and high velocity in red), as a function of Re, identified by the isosurface $\lambda_2 = -1$. (a) TE, (b) TF, and (c) TV.

APPENDIX C: WAKE STRUCTURES IDENTIFIED BY λ_2 IN THE WAKE OF A TETRAHEDRON

We present the wake structures identified by $\lambda_2 = -1$ in Fig. 28 to provide further insight into the spatial distribution of vortices and the shedding patterns in the flow past a fixed tetrahedron at three angular positions. Specifically, in the TE case at $\mathrm{Re} = 140$, we observe four vorticity threads in the wake in Fig. 25(a) that are not visible in Fig. 14. As Re increases, the DHS regime emerges and persists until $\mathrm{Re} = 360$, where the double *mushrooms* structures are clearly depicted. In contrast, the TF and TV cases exhibit two vorticity threads at low Re, leading to a nonzero lift coefficient in the PSS regime. In these cases, a single-hairpin vortex shedding occurs before the vortices become chaotic at $\mathrm{Re} = 240$ and $\mathrm{Re} = 270$, respectively. Figures 25(b) and 25(c) show that the vortex shedding plane varies with Re in the HS regime. Figure 28 demonstrates a clear transition from steady flows (MSS and PSS regimes) to unsteady flows (DHS, H, and CS regimes) and illustrates the effects of particle angular position on the pattern and the instability of the vortex structures.

[1] M. A. van der Hoef, M. van Sint Annaland, N. Deen, and J. Kuipers, Numerical simulation of dense gas-solid fluidized beds: A multiscale modeling strategy, Annu. Rev. Fluid Mech. **40**, 47 (2008).

[2] W. Zhong, A. Yu, X. Liu, Z. Tong, and H. Zhang, DEM/CFD-DEM modelling of nonspherical particulate systems: Theoretical developments and applications, Powder Technol. **302**, 108 (2016).

[3] J. Magnaudet and I. Eames, The motion of high-Reynolds-number bubbles in inhomogeneous flows, Annu. Rev. Fluid Mech. **32**, 659 (2000).
[4] T. Doychev, The dynamics of finite-size settling particles, Ph.D. thesis, Karlsruher Institut für Technologie, Germany, 2015.
[5] M. Uhlmann and T. Doychev, Sedimentation of a dilute suspension of rigid spheres at intermediate Galileo numbers: The effect of clustering upon the particle motion, J. Fluid Mech. **752**, 310 (2014).
[6] R. Williams and M. Follows, *Ocean Dynamics and the Carbon Cycle: Principles and Mechanisms* (Cambridge University Press, Cambridge, UK, 2011).
[7] L. Fréret, F. Laurant, and S. de Chaisemartin, Turbulent combustion of polydisperse evaporating sprays with droplet crossing: Eulerian modeling of collisions at finite Knudsen and validation, in *Proceedings of the Summer Program* (Center for Turbulence Research, Stanford/NASA, 2008), pp. 277–288.
[8] G. Gai, S. Kudriakov, B. Rogg, A. Hadjadj, E. Studer, and O. Thomine, Numerical study on laminar flame velocity of hydrogen-air combustion under water spray effects, Int. J. Hydrog. Energy **44**, 17015 (2019).
[9] S. Taneda, Experimental investigation of the wake behind a sphere at low Reynolds numbers, J. Phys. Soc. Jpn. **11**, 1104 (1956).
[10] I. Nakamura, Steady wake behind a sphere, Phys. Fluids **19**, 5 (1976).
[11] M. Kiya, H. Ishikawa, and H. Sakamoto, Near-wake instabilities and vortex structures of three-dimensional bluff bodies: A review, J. Wind Eng. Ind. Aerodyn. **89**, 1219 (2001).
[12] F. Cocetta, M. Gillard, J. Szmelter, and P. K. Smolarkiewicz, Stratified flow past a sphere at moderate Reynolds numbers, Comput. Fluids **226**, 104998 (2021).
[13] R. Magarvey and R. Bishop, Transition ranges for three-dimensional wakes, Can. J. Phys. **39**, 1418 (1961).
[14] T. Johnson and V. Patel, Flow past a sphere up to a Reynolds number of 300, J. Fluid Mech. **378**, 19 (1999).
[15] H. Sakamoto and H. Haniu, The formation mechanism and shedding frequency of vortices from a sphere in uniform shear flow, J. Fluid Mech. **287**, 151 (1995).
[16] B. Pier, Local and global instabilities in the wake of a sphere, J. Fluid Mech. **603**, 39 (2008).
[17] M. Jenny, J. Dušek, and G. Bouchet, Instabilities and transition of a sphere falling or ascending freely in a Newtonian fluid, J. Fluid Mech. **508**, 201 (2004).
[18] A. Tomboulides and S. Orszag, Numerical investigation of transitional and weak turbulent flow past a sphere, J. Fluid Mech. **416**, 45 (2000).
[19] R. Natarajan and A. Acrivos, The instability of the steady flow past spheres and disks, J. Fluid Mech. **254**, 323 (1993).
[20] L. Klotz, S. Goujon-Durand, J. Rokicki, and J. Wesfreid, Experimental investigation of flow behind a cube for moderate Reynolds numbers, J. Fluid Mech. **750**, 73 (2014).
[21] P. Szaltys, M. Chrust, A. Przadka, S. Goujon-Durand, L. Tuckerman, and J. Wesfreid, Nonlinear evolution of instabilities behind spheres and disks, J. Fluids Struct. **27**, 743 (2011).
[22] S. Martin, Frazil ice in rivers and oceans, Annu. Rev. Fluid Mech. **13**, 379 (1981).
[23] S. Whitaker, Forced convection heat transfer correlations for flow in pipes, past flat plates, single cylinders, single spheres, and for flow in packed beds and tube bundles, AIChE J. **18**, 361 (1972).
[24] J. Gabitto and C. Tsouris, Drag coefficient and settling velocity for particles of cylindrical shape, Powder Technol. **183**, 314 (2008).
[25] E. Loth, Drag of nonspherical solid particles of regular and irregular shape, Powder Technol. **182**, 342 (2008).
[26] A. Richter and P. Nikrityuk, Drag forces and heat transfer coefficients for spherical, cuboidal and ellipsoidal particles in cross flow at subcritical Reynolds numbers, Int. J. Heat Mass Transf. **55**, 1343 (2012).
[27] A. Seyed-Ahmadi and A. Wachs, Sedimentation of inertial monodisperse suspensions of cubes and spheres, Phys. Rev. Fluids **6**, 044306 (2021).
[28] H. Jiang and L. Cheng, Flow separation around a square cylinder at low to moderate Reynolds numbers, Phys. Fluids **32**, 044103 (2020).
[29] A. Saha, Three-dimensional numerical simulations of the transition of flow past a cube, Phys. Fluids **16**, 1630 (2004).

[30] M. Rahmani and A. Wachs, Free falling and rising of spherical and angular particles, Phys. Fluids **26**, 083301 (2014).
[31] A. Seyed-Ahmadi and A. Wachs, Dynamics and wakes of freely settling and rising cubes, Phys. Rev. Fluids **4**, 074304 (2019).
[32] M. Khan, A. Sharma, and A. Agrawal, Simulation of flow around a cube at moderate Reynolds numbers using the lattice Boltzmann method, J. Fluids Eng. **142**, 011301 (2019).
[33] R. Raul, P. Bernard, and F. T. Buckley, Jr., An application of the vorticity-vector potential method to laminar cube flow, Int. J. Numer. Methods Fluids **10**, 875 (1990).
[34] A. Saha, Three-dimensional numerical study of flow and heat transfer from a cube placed in a uniform flow, Int. J. Heat Fluid Flow **27**, 80 (2006).
[35] Q. Meng, H. An, L. Cheng, and M. Kimiaei, Wake transitions behind a cube at low and moderate Reynolds numbers, J. Fluid Mech. **919**, A44 (2021).
[36] Y. Lim, P. Wang, J. Yeo, and S. Yu, Experimental and numerical studies for flow over a Sierpinski tetrahedron for potential windbreak application, J. Wind. Eng. Ind. Aerodyn. **216**, 104712 (2021).
[37] A. Haider and O. Levenspiel, Drag coefficient and terminal velocity of spherical and nonspherical particles, Powder Technol. **58**, 63 (1989).
[38] E. Pettyjohn and E. Christiansen, Effect of particle shape on free settling rates of isometric particles, Chem. Eng. Prog. **44**, 157 (1948).
[39] D. Leith, Drag on nonspherical objects, Aerosol Sci. Technol. **6**, 153 (1987).
[40] K. Wittig, A. Richter, and P. Nikrityuk, Numerical study of heat and fluid flow past a cubical particle at subcritical Reynolds numbers, Comp. Thermal Sciences **4**, 283 (2012).
[41] G. Ganser, A rational approach to drag prediction of spherical and nonspherical particles, Powder Technol. **77**, 143 (1993).
[42] A. Hölzer and M. Sommerfeld, New simple correlation formula for the drag coefficient of nonspherical particles, Powder Technol. **184**, 361 (2008).
[43] A. Hölzer and M. Sommerfeld, Lattice Boltzmann simulations to determine drag, lift, and torque acting on nonspherical particles, Comput. Fluids **38**, 572 (2009).
[44] J. McNown and J. Malaika, Effects of particle shape on settling velocity at low Reynolds numbers, Trans. AGU **31**, 74 (1950).
[45] H. Zhang, X. Bo, X. An, C. Ke, and J. Chen, Numerical prediction on the drag force and heat transfer of nonspherical particles in supercritical water, Powder Technol. **361**, 414 (2020).
[46] G. Gai and A. Wachs, Dynamics, wakes, and regime transitions of a fixed angular particle in an unbounded inertial flow. II. From tetrahedron to sphere, Phys. Rev. Fluids **8**, 064305 (2023).
[47] R. Glowinski, T. Pan, T. Hesla, and D. Joseph, A distributed Lagrange multiplier/fictitious domain method for particulate flows, Int. J. Multiphase Flow **25**, 755 (1999).
[48] A. Wachs, A DEM-DLM/FD method for direct numerical simulation of particulate flows: Sedimentation of polygonal isometric particles in a Newtonian fluid with collisions, Comput. Fluids **38**, 1608 (2009).
[49] A. Wachs, PeliGRIFF, A parallel DEM-DLM/FD direct numerical simulation tool for 3D particulate flows, J. Eng. Math. **71**, 131 (2011).
[50] A. Wachs, A. Hammouti, G. Vinay, and M. Rahmani, Accuracy of finite volume/staggered grid distributed Lagrange multiplier/fictitious domain simulations of particulate flows, Comput. Fluids **115**, 154 (2015).
[51] C. Selçuk, A. R. Ghigo, S. Popinet, and A. Wachs, A fictitious domain method with distributed Lagrange multipliers on adaptive quad/octrees for the direct numerical simulation of particle-laden flows, J. Comput. Phys. **430**, 109954 (2021).
[52] A. Seyed-Ahmadi and A. Wachs, Microstructure-informed probability-driven point-particle model for hydrodynamic forces and torques in particle-laden flows, J. Fluid Mech. **900**, A21 (2020).
[53] G. Gai and A. Wachs, High fidelity adaptive Cartesian octree grid computations of the flow past a Platonic polyhedron up to a Reynolds number of 200, Powder Technol. **420**, 118390 (2023).
[54] S. Popinet, A quadtree-adaptive multigrid solver for the Serre–Green–Naghdi equations, J. Comput. Phys. **302**, 336 (2015).
[55] J. Jeong and F. Hussain, On the identification of a vortex, J. Fluid Mech. **285**, 69 (1995).

[56] Z. Yu, N. Phan-Thien, Y. Fan, and R. Tanner, Viscoelastic mobility problem of a system of particles, J. Non-Newton. Fluid Mech. **104**, 87 (2002).
[57] A. van Hooft, S. Popinet, C. Heerwaarden, S. van der Linden, S. de Roode, and B. van de Wiel, Towards adaptive grids for atmospheric boundary-layer simulations, Boundary-Layer Meteorol. **167**, 421 (2018).
[58] See Supplemental Material at http://link.aps.org/supplemental/10.1103/PhysRevFluids.8.064304 for videos of the double-hairpin vortex shedding past a TE tetrahedron at Re=220.
[59] https://alliancecan.ca/en.
[60] G. Marchuk, Splitting and alternating direction methods, Handb. Numer. Anal. **1**, 197 (1990).
[61] R. Glowinski, T. Pan, T. Hesla, D. Joseph, and J. Periaux, A fictitious domain approach to the direct numerical simulation of incompressible viscous flow past moving rigid bodies: Application to particulate flow, J. Comput. Phys. **169**, 363 (2001).
[62] Z. Yu, N. Phan-Thien, and R. Tanner, Dynamic simulation of sphere motion in a vertical tube, J. Fluid Mech. **518**, 61 (2004).
[63] J. Lu, S. Das, E. Peters, and J. Kuipers, Direct numerical simulation of fluid flow and mass transfer in dense fluid-particle systems with surface reactions, Chem. Eng. Sci. **176**, 1 (2018).
[64] A. D. Rakotonirina, J.-Y. Delenne, F. Radjai, and A. Wachs, Grains3D, a flexible DEM approach for particles of arbitrary convex shape—Part III: Extension to nonconvex particles modelled as glued convex particles, Comput. Part. Mech. **6**, 55 (2019).
[65] A. Wachs, L. Girolami, G. Vinay, and G. Ferrer, Grains3D, a flexible DEM approach for particles of arbitrary convex shape—Part I: Numerical model and validations, Powder Technol. **224**, 374 (2012).